Bidimensional ensemble empirical mode decomposition of functional biomedical images taken during a contour integration task

S. Al-Baddai [a,b], K. Al-Subari [a,b], A.M. Tomé [c], G. Volberg [d], S. Hanslmayr [e], R. Hammwöhner [b], E.W. Lang [a,*]

[a] CIML Group, Biophysics, University of Regensburg, 93040 Regensburg, Germany
[b] Information Sciences, University of Regensburg, Germany
[c] IEETA, DETI, Universidade de Aveiro, 3810 Aveiro, Portugal
[d] Experimental Psychology, University of Regensburg, Germany
[e] Cognition and Oscillations Lab, Department of Psychology, University of Konstanz, Germany

ARTICLE INFO

ABSTRACT

In cognitive neuroscience, extracting characteristic textures and features from functional imaging modalities which could be useful in identifying particular cognitive states across different conditions is still an important field of study. This paper explores the potential of two-dimensional ensemble empirical mode decomposition (2DEEMD) to extract such textures, so-called bidimensional intrinsic mode functions (BIMFs), of functional biomedical images, especially functional magnetic resonance images (fMRI) taken while performing a contour integration task. To identify most informative textures, i.e. BIMFs, a support vector machine (SVM) as well as a random forest (RF) classifier is trained for two different stimulus/response conditions. Classification performance is used to estimate the discriminative power of extracted BIMFs. The latter are then analyzed according to their spatial distribution of brain activations related with contour integration. Results distinctly show the participation of frontal brain areas in contour integration. Employing features generated from textures represented by BIMFs exhibit superior classification performance when compared with a canonical general linear model (GLM) analysis employing statistical parametric mapping (SPM).

© 2014 Elsevier Ltd. All rights reserved.

1. Introduction

The increasing importance of functional imaging techniques in cognitive brain studies creates the need for adapting modern data mining and machine learning methods to the specific requirements of biomedical images, most notably functional magnetic resonance imaging techniques (fMRI). The latter are able to reveal neural processing and cognitive states during cognitive task performance. Also fMRI can be applied repeatedly as it does not apply harmful ionizing radiation to subjects [62,20]. The resulting large volume of such image series renders their analysis and interpretation tedious. This creates the need for robust and automatized techniques to extract the information buried in such images, to analyze them objectively and to classify them properly. Brain mapping using magnetic resonance imaging (MRI) is traditionally performed using voxel-wise statistical hypothesis testing. It is typically based on β – images resulting from a linear regression analysis, calculated by powerful tools like the widely used *statistical parametric mapping* (SPM). Such univariate approach ignores subtle spatial interactions. Alternatively, *exploratory matrix factorization* (EMF) techniques like independent component analysis (ICA) [8,10] and nonnegative matrix and tensor factorization (NMF/NTF) [11] provide a more global analysis taking such interactions into account. In general, voxel time courses, or corresponding spatial variations, of activity distributions in fMRI images represent nonlinear and non-stationary signals.

Recently, an empirical nonlinear analysis tool for such complex, non-stationary spatio-temporal signal variations has been pioneered by Huang et al. [23]. Afterwards an extension to multidimensional spatio-temporal signal variations was put forward by Nunes et al. [45], Mandic et al. [49] and, recently, especially by Wu et al. [64]. Such techniques are commonly referred to as *empirical mode decomposition* (EMD), and if combined with Hilbert spectral analysis, they are called *Hilbert–Huang transform* (HHT). They adaptively and locally decompose any non-stationary signal in a sum of intrinsic mode functions (IMF) which represent zero-mean, amplitude and (spatial-) frequency modulated components. EMD, and its two-dimensional counterpart 2DEMD, represent a fully

---

data-driven, unsupervised signal decomposition which does not need any *a priori* defined basis system like Fourier- or Wavelet-based techniques. Furthermore, EMD satisfies the perfect reconstruction property. Thus it lacks the scaling and permutation indeterminacy familiar from blind source separation (BSS) techniques [12]. Owing to these characteristics, 2DEMD, and even more so its noise-assisted variant called *ensemble empirical mode decomposition* (2DEEMD), is highly promising in analyzing such spatio-temporal signal variations of a multi-scale nature. Note that, for fMRI purposes, EEMD could be even extended to a full 3D-EEMD of a whole brain volume, or even 4D-EEMD if time should be included as well. However, the computational load would increase considerably then which renders such analyses still impractical with large data sets.

If two-dimensional IMFs, which represent the same spatial scale, are combined to more global bidimensional IMFs, henceforth called BIMFs, the latter reveal characteristic underlying textures of the multivariate spatio-temporal activity distributions, and provide proper features for classification purposes. Such automated feature extraction proofs especially useful in cognitive neuroscience research for later stimulus response classification. Only few studies have been performed yet to apply multi-dimensional EMD to biomedical images. Zheng et al. [69] reported the use of EMD for activation detection in fMRI images of the brain. Rojas et al. [53] report on applying EMD to Single Photon Emission Computed Tomography (SPECT) images to explore Parkinson's disease. Also very recently, Zemzami et al. [67] used a bi-dimensional EMD approach to decompose 3D biomedical magnetic resonance images (MRI) into bi-dimensional IMFs which then have been reconstructed into 3D volume image modes. Deng et al. [14] recently proposed an new method for fMRI analysis based on empirical mean curve decomposition. Kriegeskorte et al. [29] used *searchlight* approaches which use a multivariate predictive model in each local neighborhood in brain space. The classification performance is then reported at the center of the searchlight to build an information map. Also classification methods that analyze the brain as a whole, based on an SPM analysis, have been tested (e.g. [21,41]). Lately, there has been a growing interest in state-of-the-art feature extraction techniques for investigating whether stimulus information is present in fMRI response patterns, and attempting to decode the stimuli from the response patterns with a multivariate classifier. However, little is known about the relative performance of different classifiers on fMRI data. These techniques have been successfully applied to the individual classification of a variety of neurological conditions [31,16,26,61], and allow capturing complex multivariate relationships in the data. Multivariate machine learning methods allow for multi-voxel pattern analysis and can reveal patterns amongst voxels in fMRI data [22,43], and so may provide much more detailed information about brain activity, i.e. not only local increases but distributed patterns of activity are identified.

This paper explores the potential of 2DEEMD to decompose fMRI images recorded while performing a cognitive task, more specifically a contour integration task while viewing oriented Gabor patches presented as visual stimuli. Further post-processing serves to reduce the dimension of the data sets and to transform the component images according to additional statistical constraints like orthogonality or independence. Feature quality is assessed by statistical measures of properly trained SVM and RF classifiers. First various parameters of the method like the number of sifting steps, the amplitude of added white noise, the number of extracted BIMFs, etc., of the algorithm need to be varied systematically to develop strategies for determining respective optimal values, followed by employing 2DEEMD to extract characteristic textures on different spatial scales. In a second step, features generated from the related volume intrinsic mode functions (VIMFs) are fed into the classifiers. The classifiers serve to corroborate the discriminative power of the extracted features, and by way of proper statistical measures, component images most discriminative for decision making can be identified. Subsequently, activity distributions related to these BIMFs or VIMFs, respectively, can be analyzed with respect to activated brain areas involved and available knowledge about visual processing and contour integration accumulated in the open literature. As during the scan the subjects are asked to indicate the presence or absence of a contour in the stimulus pattern, there are two classes to differentiate: *contour true* (CT) and *non-contour true* (NCT). From these results the performance of the classifiers as well as the sensitivity and specificity of their responses, can be deduced. These classification results will reveal those component images and their concomitant neuronal activity distributions, which best differentiate between the classes hence contain the most information as to where neuronal activations are localized in the brain which operate on contour integration tasks within visual processing.

2. Theory – empirical mode decomposition

2.1. Background

Roughly a decade ago, an empirical nonlinear analysis tool for complex, non-stationary time series has been pioneered by Huang et al. [23]. It is commonly referred to as *empirical mode decomposition* (EMD) and if combined with Hilbert spectral analysis it is called *Hilbert–Huang transform* (HHT). It can be applied to any non-stationary and also nonlinear data set and represents a heuristic data decomposition technique which adaptively and locally decomposes any non-stationary time series in a sum of *intrinsic mode functions* (IMF) which represent zero-mean amplitude and frequency modulated components. The EMD represents a fully data-driven, unsupervised signal decomposition and does not need any *a priori* defined basis system. EMD also assures perfect reconstruction, i.e. superimposing all extracted IMFs together with the residual trend reconstructs the original signal without information loss or distortion. However, if only partial reconstruction is intended, it is not based on any optimality criterion rather on a binary *include* or *not include* decision. The empirical nature of EMD offers the advantage over other signal decomposition techniques like *exploratory matrix factorization* (EMF) [30] of not being constrained by conditions which often only apply approximately. Especially with cognitive signal processing, one often has only a rough idea about the underlying modes or component images, and frequently their number is unknown.

Eventually, the original signal $x(t)$ can be expressed as

$$x(t) = \sum_j c^{(j)}(t) + r(t)$$

$$c^{(j)}(t) = Re\{a_j(t)\exp(i\phi_j(t))\} = Re\{a_j(t)\exp(i\int_{-\infty}^{t}\omega_j(t')dt')\} \tag{1}$$

where the $c^{(j)}(t)$ represent the IMFs and $r(t)$ the remaining non-oscillating trend. Furthermore, $a_j(t)$ denotes a time-dependent amplitude, $\phi_j(t) = \int \omega_j(t)dt$ represents a time-dependent phase and $\omega_j[rad/s] = (d\phi_j(t))/(dt)$ denotes the related instantaneous frequency. Plotting both amplitude $a_j(t)$ and phase $\phi_j(t)$ as a function of time for each extracted IMF represents a *Hilbert–Huang spectrogram* [4].

During sifting, mode mixing as well as boundary artifacts can be avoided by a variant called *ensemble empirical mode decomposition* (EEMD) which has been introduced by Wu and Huang [63]. It represents a noise-assisted data analysis method. First white noise of finite amplitude is added to the data, and then the EMD algorithm is applied. This procedure is repeated many times, and the IMFs are

calculated as the mean of an ensemble, consisting of the signal and added white noise. With a growing ensemble number, the IMF converges to the true IMF [63]. Adding white noise to the data can be considered a physical experiment which is repeated many times. The added noise is treated as random noise, which appears in the measurement. In this case, the nth noisy observation will be

$$x_n(t) = x(t) + \epsilon_n(t) = \sum_j c_n^{(j)}(t) + r_n(t), \tag{2}$$

where $x(t)$ is the true signal, $\epsilon_n(t)$ is the random noise and $c_n^{(j)} = c^{(j)} + \epsilon_n(t)$ represents the IMF obtained for the nth noise observation. For the sake of simplicity, following we denote the residuum as $r_n(t) \equiv c_n^{(J)}(t)$, hence formally include it into the summation over the IMFs.

Soon after its invention, EMD has been extended to higher dimensions [44,64,49,48,50,19] including complex-valued data sets [59,1,38]. Obviously, two-dimensional image data sets were of special interest [51]. In a first approach, such two-dimensional data was treated as a collection of one-dimensional slices, which were decomposed with one-dimensional EMD. This procedure is called *pseudo-two-dimensional EMD* [64]. However, pseudo-2D-EMD needs a coherence structure associated with the spatial scales in a particular direction, which significantly limits its use. These recent developments in analysis methods for non-linear and non-stationary data sets have received considerable attention by image analysts. Thus several attempts have been started lately to extend EMD to multi-array data sets like two-dimensional (2D) data arrays and images. These extensions are variously known as *bidimensional EMD* (BEMD), *image EMD* (IEMD), *2D EMD* and so on [44–46,33,13,66,35,36,65]. The most demanding operation of these algorithms involves an envelope surface interpolation step. In [13] the influence of various interpolation methods is studied, and a *sifting* process is proposed based on a Delaunay triangulation with subsequent cubic interpolation on triangles. In [5,6] the envelope surface interpolation step is replaced by either a direct envelope surface estimation method or radial basis function interpolators. Finally, the modified 2D EMD algorithm proposed in [65] implements the FastRBF algorithm in an estimation of the envelope surfaces. Some of these works exploit decompositions to compute texture information contained in the images. In [68] a new two-dimensional EMD (2DEMD) method is proposed, which is claimed being faster and better-performing than current 2DEMD methods. In [65] rotation-invariant texture feature vectors are extracted at multiple scales or spatial frequencies based on a BEMD. In Nunes et al. [44–46] the BEMD-based texture extraction algorithm is demonstrated in experiments with both synthetic and natural images. Textures are an especially relevant feature of biomedical images if their subsequent classification is intended as is the goal of this study also.

Besides a genuine 2D implementation of the BEMD process, 1D EMD has also been applied to images to extract 2D IMFs or bidimensional IMFs (BIMFs) [36,37]. The latter technique treats each row and/or each column of the 2D data set separately by a 1D EMD, which renders the sifting process faster than in a genuine 2D decomposition. But this parallel 1D implementation results in poor BIMF components compared to the standard 2D procedure due to the fact that the former ignores the correlation among the rows and/or columns of a 2D image [34]. A major breakthrough has been achieved by Wu et al. [64], who recently proposed a *multidimensional ensemble empirical mode decomposition* (MEEMD) for multidimensional data arrays. The well-known ensemble empirical mode decomposition (EEMD) is applied to slices of data in each and every dimension involved. The combination of partial IMFs to the final multi-dimensional IMF is based on a *comparable minimal scale combination principle* (CMSC-principle). Note that the spatial frequencies of the characteristic textures of the extracted BIMFs are related in correspondence with a dyadic filter bank property of the EMD analysis [18]. MEEMD turned out to be very efficient in practical applications, especially if applied to the two-dimensional case, and will be used in this work to analyze fMRI images taken while subjects were performing a cognitive task. Hence, a short summary of the method, introducing the notation used further on, will be given in the following for the convenience of the reader.

2.2. Two-dimensional ensemble empirical mode decomposition

Analyzing 2D data arrays, for example an fMRI brain slice, one starts by applying EEMD to each column $X_{*n} \equiv \mathbf{x}_n$ of the $M \times N$ – dimensional data matrix $\mathbf{X}$

$$\mathbf{X} = [x_{m,n}] = \begin{bmatrix} x_{1,1} & x_{1,2} & \cdots & x_{1,N} \\ x_{2,1} & x_{2,2} & \cdots & x_{2,N} \\ \vdots & \vdots & \cdots & \vdots \\ x_{M,1} & x_{M,2} & \cdots & x_{M,N} \end{bmatrix} \tag{3}$$

The 1D-EEMD decomposition of the nth column becomes

$$\mathbf{x}_n := X_{*,n} = \sum_{j=1}^{J} C_{*,n}^{(j)} = \sum_{j=1}^{J} \begin{pmatrix} c_{1,n}^{(j)} \\ c_{2,n}^{(j)} \\ \vdots \\ c_{M,n}^{(j)} \end{pmatrix} \tag{4}$$

where the column vector $C_{*,n}^{(J)}$ represents the residuum of the nth column vector of the data matrix. This finally results in J component matrices, each one containing the jth component of every column $\mathbf{x}_n$, $n = 1, \ldots, N$ of the data matrix $\mathbf{X}$.

$$\mathbf{C}^{(j)} = [\, \mathbf{c}_1^{(j)} \quad \mathbf{c}_2^{(j)} \quad \cdots \quad \mathbf{c}_N^{(j)} \,] = [\, C_{*,1}^{(j)} \quad C_{*,2}^{(j)} \quad \cdots \quad C_{*,N}^{(j)} \,]$$

$$= \begin{bmatrix} c_{1,1}^{(j)} & c_{1,2}^{(j)} & \cdots & c_{1,N}^{(j)} \\ c_{2,1}^{(j)} & c_{2,2}^{(j)} & \cdots & c_{2,N}^{(j)} \\ \vdots & \vdots & \cdots & \vdots \\ c_{M,1}^{(j)} & c_{M,2}^{(j)} & \cdots & c_{M,N}^{(j)} \end{bmatrix} \tag{5}$$

Next one applies an EEMD to each row of Eq. (5) yielding

$$C_{m,*}^{(j)} = (\, c_{m,1}^{(j)} \quad c_{m,2}^{(j)} \quad \cdots \quad c_{m,N}^{(j)} \,) = \sum_{k=1}^{K} (\, h_{m,1}^{(j,k)} \quad h_{m,2}^{(j,k)} \quad \cdots \quad h_{m,N}^{(j,k)} \,)$$

$$= \sum_{k=1}^{K} H_{m,*}^{(j,k)} \tag{6}$$

where $c_{m,n}^{(j)} = \sum_{k=1}^{K} h_{m,n}^{(j,k)}$ represents the decomposition of the rows of matrix $\mathbf{C}^{(j)}$. These components $h_{m,n}^{(j,k)}$ can be arranged into a matrix $\mathbf{H}^{(j,k)}$ according to

$$\mathbf{H}^{(j,k)} = \begin{bmatrix} h_{1,1}^{(j,k)} & h_{1,2}^{(j,k)} & \cdots & h_{1,N}^{(j,k)} \\ h_{2,1}^{(j,k)} & h_{2,2}^{(j,k)} & \cdots & h_{2,N}^{(j,k)} \\ \vdots & \vdots & \cdots & \vdots \\ h_{M,1}^{(j,k)} & h_{M,2}^{(j,k)} & \cdots & h_{M,N}^{(j,k)} \end{bmatrix} \tag{7}$$
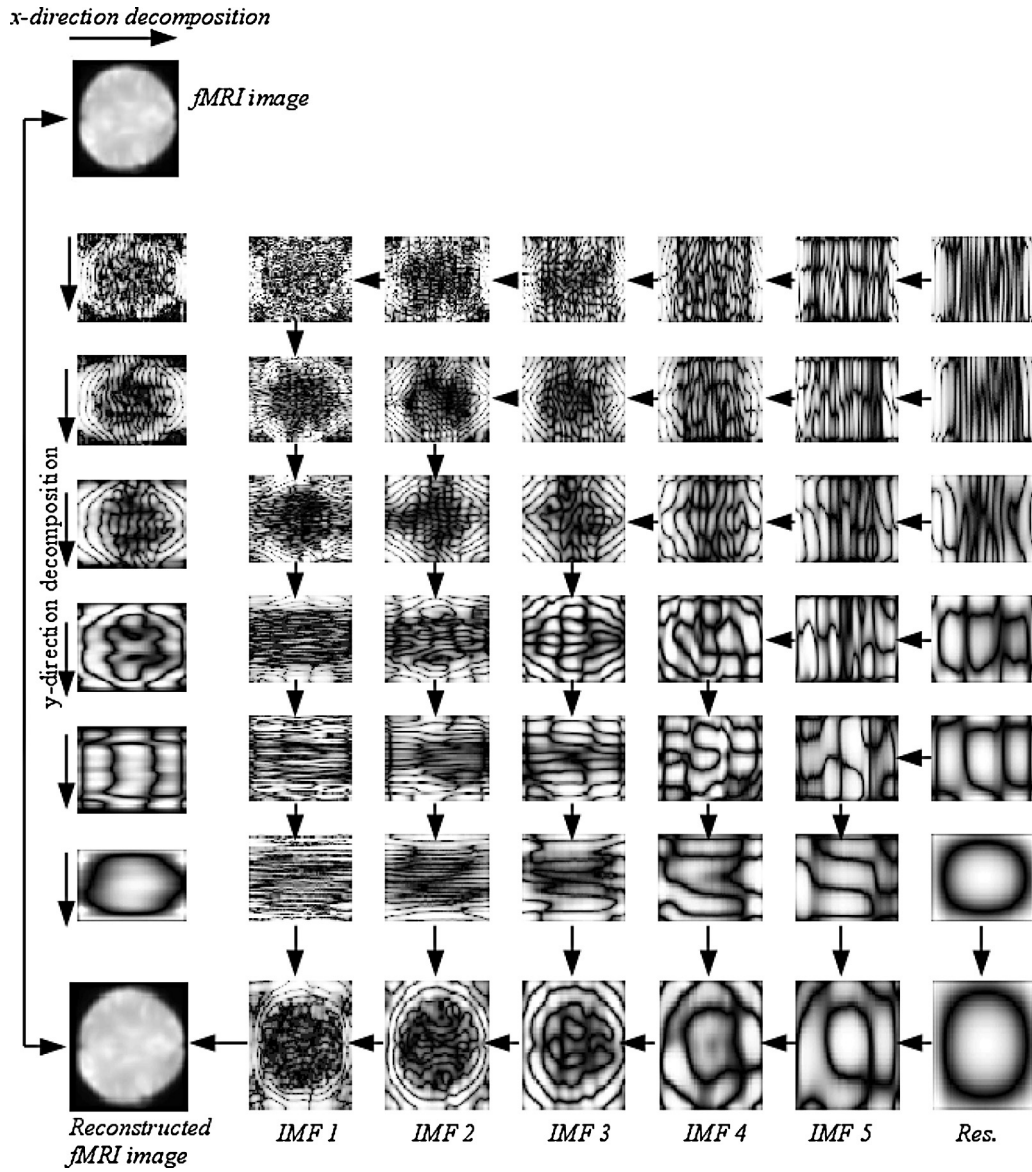
Fig. 1. An illustration of the 2DEEMD decomposition of an fMRI image. IMFs along each row or column represent textures of comparable scale and are to be summed up to yield a BIMF. To improve visibility, histogram equalization has been applied on each image separately.

The resulting component matrices have to be summed to obtain

$$\mathbf{C}^{(j)} = \sum_{k=1}^{K} \mathbf{H}^{(j,k)}. \tag{8}$$

Finally this yields the following decomposition of the original data matrix $\mathbf{X}$

$$\mathbf{X} = \sum_{j=1}^{J} \mathbf{C}^{(j)} = \sum_{j=1}^{J} \sum_{k=1}^{K} \mathbf{H}^{(j,k)} \tag{9}$$

where each element is given by

$$x_{m,n} = \sum_{j=1}^{J} \sum_{k=1}^{K} h_{m,n}^{(j,k)} \tag{10}$$

To yield meaningful results, components $h_{m,n}^{(j,k)}$ with comparable scales, i.e. similar spatial frequencies of their textures, should finally be combined [64]. Note, that the CMSC-principle affords to have $K = J$. In practice, for two-dimensional data sets this implies

that the components of each row, which represent a common horizontal scale, and the components of each column, which represent a common vertical scale, should be summed up [64].

Hence, the CMSC – principle leads to BIMFs given by

$$\mathbf{S}^{(k\prime)} = \sum_{k=1}^{K} \mathbf{H}^{(k,k\prime)} + \sum_{j=k\prime+1}^{J} \mathbf{H}^{(k\prime,j)} \tag{11}$$

which thus yields a decomposition of the original data matrix $\mathbf{X}$ into BIMFs according to

$$\mathbf{X} = \sum_{k\prime=1}^{K} \mathbf{S}^{(k\prime)} \tag{12}$$

where $\mathbf{S}^{(K)}$ represents the non-oscillating residuum. The extracted BIMFs can be considered features of the data set which, according to the CMSC – principle, reveal local textures with characteristic spatial frequencies which help to discriminate the functional images under study.

Fig. 1 illustrates the 2DEEMD and the CMSC – principle in case of a decomposition of an fMRI image. It clearly describes the steps
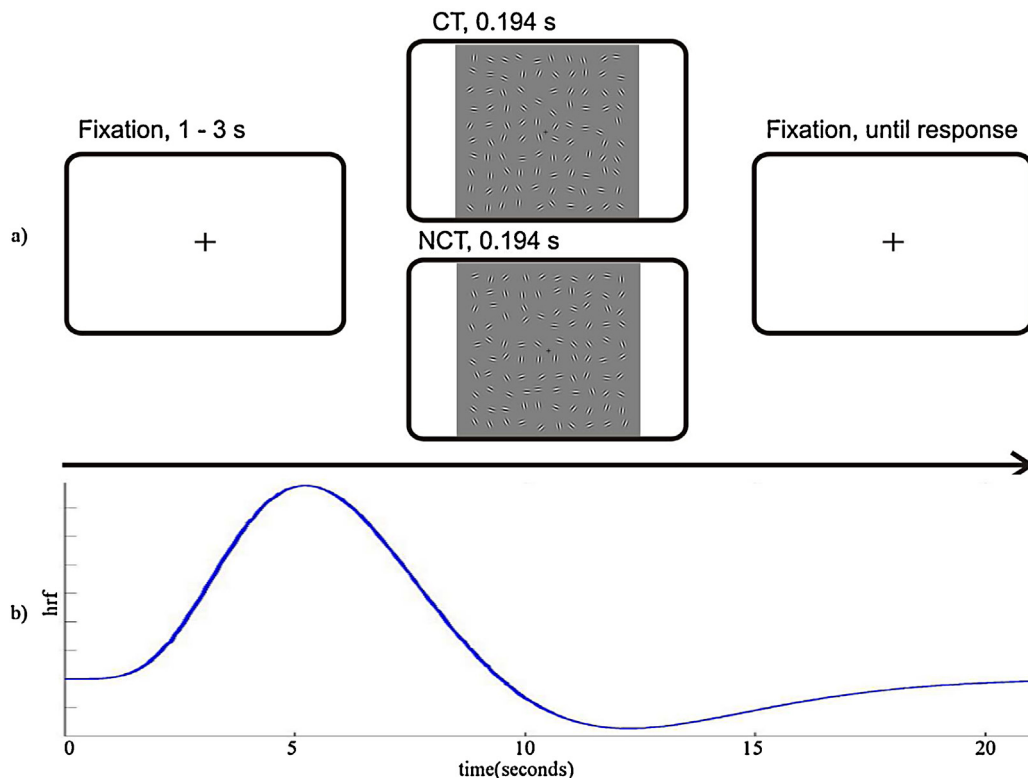
Fig. 2. Stimuli and stimulus design: (a) stimulus protocol and Gabor patches either forming a contour line (CT) or not (NCT), (b) prototypical hemodynamic response function (HRF).

of the 2DEEMD algorithm using an fMRI image, i.e. a single brain slice, as an example. The image presented in the upper left corner represents the original fMRI image. The first column on the left side, with the exception of the original image in the upper left corner and the reconstructed image represented on the bottom left side, represents the component images resulting from decompositions along the x-direction. The columns $2 \rightarrow 6$, except the last row, represent the component images resulting from a decomposition along the y-direction of each component image which resulted from a decomposition along the x-dimension. The last row, except the reconstructed image on the bottom left side, represents the final BIMFs of the original fMRI image obtained by applying the CMSC – principal.

3. Materials

3.1. Experimental setup

In this study, functional images were recorded with a 3-Tesla head scanner (Siemens Allegra, Erlangen, Germany) at the courtesy of Prof. M. Greenlee, Experimental Psychology, University of Regensburg, Germany. For the functional series whole brain images were continuously acquired with 46 interleaved axial slices using a standard T_{2^*}-weighted echo-planar imaging sequence employing the following parameters: repetition time $TR = 2000$ ms; echo time $TE = 30$ ms; flip angle $\theta = 90°$; 64×64 matrices; in-plane resolution: 3 mm × 3 mm; slice thickness: 3 mm. After the functional scans, high-resolution sagittal T_1-weighted images were acquired for obtaining a 3D structural scan, using a magnetization prepared rapid gradient echo sequence ($MP - RAGE$) and employing the following parameters: $TR = 2250$ ms; $TE = 2.6$ ms; 1 mm isotropic voxel size. This sequence is optimized to differentiate between white and gray matter. Subjects were positioned supine in the scanner with

their head secured in the head coil to minimize head movement. Visual stimuli were presented, using the software package *Presentation* 12.0 (Neurobehavioral Systems Inc., Albany, Canada), on a standard PC equipped with a 3D graphics card, and back-projected via an LCD video projector (JVC, DLA-G20, Yokohama, Japan) onto a translucent circular screen. The stimuli were seen on a mirror reflecting the image from the projection screen. The projector had a resolution of 800 × 600 pixels and a refresh rate of 72 Hz. The viewing distance to the projection screen was 64 cm. Participants were subjected to a perceptual detection task, see Fig. 2. In each trial, a visual stimulus was presented for 194 ms, followed by a blank screen. In half of the stimuli, some Gabor patches formed contours as targets to be detected, while the rest of the patches were oriented randomly as was the case in all the remaining stimuli. Each stimulus array contained 90–100 Gabor patterns and subtended 16.6 by 16.5° of visual angle. A cohort of 19 subjects has been studied during 3 sessions, each encompassing numerous ($\lesssim$150) trials with Gabor stimuli, organized in 5 blocks. In each trial, the subjects classified the stimulus as *contour* or *non-contour* by pressing an associated response button with either the left of the right hand. This resulted in 4 conditions: (1) there was a contour and the subject recognized it correctly (decoded as CT), (2) there was a contour and the subject did not recognize it (decoded as CF), (3) there was no contour but the subject falsely recognized a contour (decoded as NCF) and (4) there was no contour and the subject recognize its absence correctly (decoded as NCT). In this study we concentrate on the two conditions CT and NCT, only as for the other two conditions far less trials were available.

Functional data were preprocessed with the software package *SPM8* (Wellcome Department of Imaging Neuroscience, London, UK), running under MATLAB 7.0 (Mathworks, Natick, MA). This preprocessing included slice-time correction, motion-correction, spatial normalization and spatial Gaussian smoothing. Except from
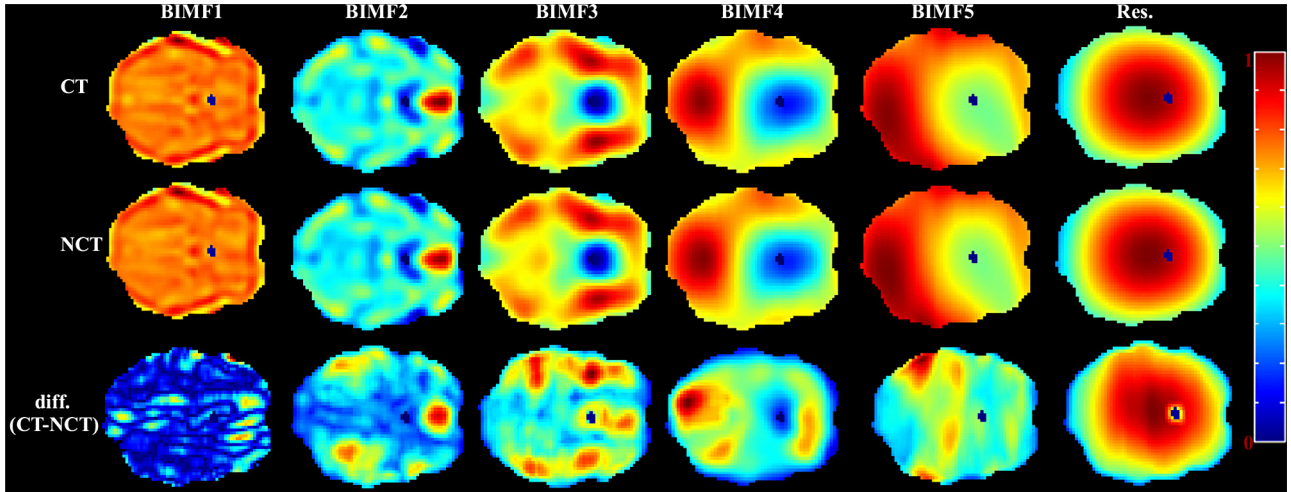
Fig. 3. Illustration of the BIMFs resulting from an 2DEEMD decomposition of a single brain slice for both stimulus conditions, i.e. CT and NCT. Note that BIMFs for both conditions have been normalized to the same scale to render them comparable, while the difference images have been normalized separately for enhancing visibility of small differences.

this no further pre-processing has been considered and these "raw" images have been analyzed.

3.2. Data set

Note that with fMRI recordings, the brain is scanned in a number of slices, here ($N_s = 46$), which together comprise a 3D activity distribution, henceforth called a volume of activations. Each such brain slice represents a 2D data array which is decomposed by 2DEEMD into $K = 6$ BIMFs per slice. Fig. 3 illustrates corresponding results for a single brain slice. Note that the BIMFs for both conditions have been normalized jointly to render their relative activation levels comparable, but that the resulting difference BIMFs have been normalized separately to enhance visibility of sometimes small differences.

Given there are $N_c = 790$ scans per session, each one comprising $N_s = 46$ brain slices, we consider each *complete scan*, further on called *volume scan*, as being equivalent to a data volume $V_c(x, y, z)$ where x, y, z denote the spatial coordinates of the voxels in the brain volume. Here index c counts these scans, thus forming an index set $\{C | c \in \mathbb{N}, c = 1, \ldots, 790\}$. Now choose the subset of indices corresponding to those volume scans acquired during the time when the hemodynamic response (HR) appeared after the stimulus onset. The HR usually happens roughly $\tau \approx 5$ s after the stimulus onset. So, for any given stimulus/response condition, the term *trials* corresponds to those volume scans registered while the hemodynamic response was active. For each of the conditions *contour true* (CT) and *non-contour true* (NCT) there were $N_t \approx 90$–120 trials across all three sessions, corresponding to an equal number of volume scans.

To summarize, the whole data set being analyzed is thus characterized by the following parameters:

- the number of slices per volume: $N_s = 46$
- the number of voxels per slice: $N_{vs} = 53 \times 63 = 3339$
- the number of stimulus conditions analyzed: $N_{st} = 2$, corresponding to the conditions CT – contour true, NCT – non-contour true
- the number of trials per condition: $90 \le N_t \le 120$
- the number of subjects analyzed: $N_{sj} = 19$
- the number of voxels per volume: $R = N_s \times N_{vs}$
- the size of the analyzed data set: $S = N_{sj} \times N_{st} = 38$

To reduce the computational load, per condition, these volume scans were averaged, yielding one *volume of average activations* per

condition and session $\langle V_{sc}(x, y, z) \rangle$ according to

$$\bar{V}(x, y, z) \equiv \langle V_{sc}(x, y, z) \rangle = \frac{1}{N_t} \sum_{sc \in C} V_{sc \in C}(x, y, z)$$

where $sc \in C$ denotes those indices of the volumes, belonging to stimulus condition $sc \in \{CT, NCT\}$. Note that $\langle V_{sc \in C}(x, y, z = n_s) \rangle \equiv \mathbf{X}_{n_s}$ represents an average brain slice to be decomposed by 2DEEMD (see Eq. (12)) into K BIMFs. If repeated for all brain slices $\mathbf{X}_{n_s}$, $n_s = 1, \ldots, N_s$, this decomposition results in K *volume intrinsic mode functions VIMFk*, $k = 1, \ldots, K$. For further processing, each VIMF is concatenated into a column vector.

4. Methods

4.1. 2D-EEMD parameter estimation for fMRI images

Despite the introduction of VIMFs, the 2*DEEMD* decomposition has been performed at the level of average brain slices. As was already mentioned in the introduction, proper parameters, such as the number of sifting steps, the ensemble size, the noise amplitude etc., have to be assigned before one can apply 2*DEEMD* to fMRI images. Thus in this study, the space of parameters has been explored in a systematic fashion to decide on appropriate values for each parameter as is discussed in the following paragraphs.

4.1.1. Number of sifting steps

For rendering decompositions comparable, one cannot use a stopping criterion which is deduced from the data as then each BIMF of a brain slice $\mathbf{X}_{n_s}$ will result from a different number of sifting steps. Then the BIMFs will vary in each slice and their comparison will be unjust. It is common experience that only a small number of sifting steps is needed usually to extract a proper BIMF. Huang et al. [23] suggest that 15 sifting steps should be sufficient to create reliable BIMFs. To check this assertion, trial decompositions have been performed where sifting was stopped whenever a residuum resulted. From these experiments it was verified that indeed 15 sifting steps sufficed to achieve a stable and reproducible decomposition, except for the lowest spatial frequency modes. In addition, note that with a larger number of sifting steps no improvement of the resulting modes could be observed but the computational load is strongly increased. So as a good compromise between image
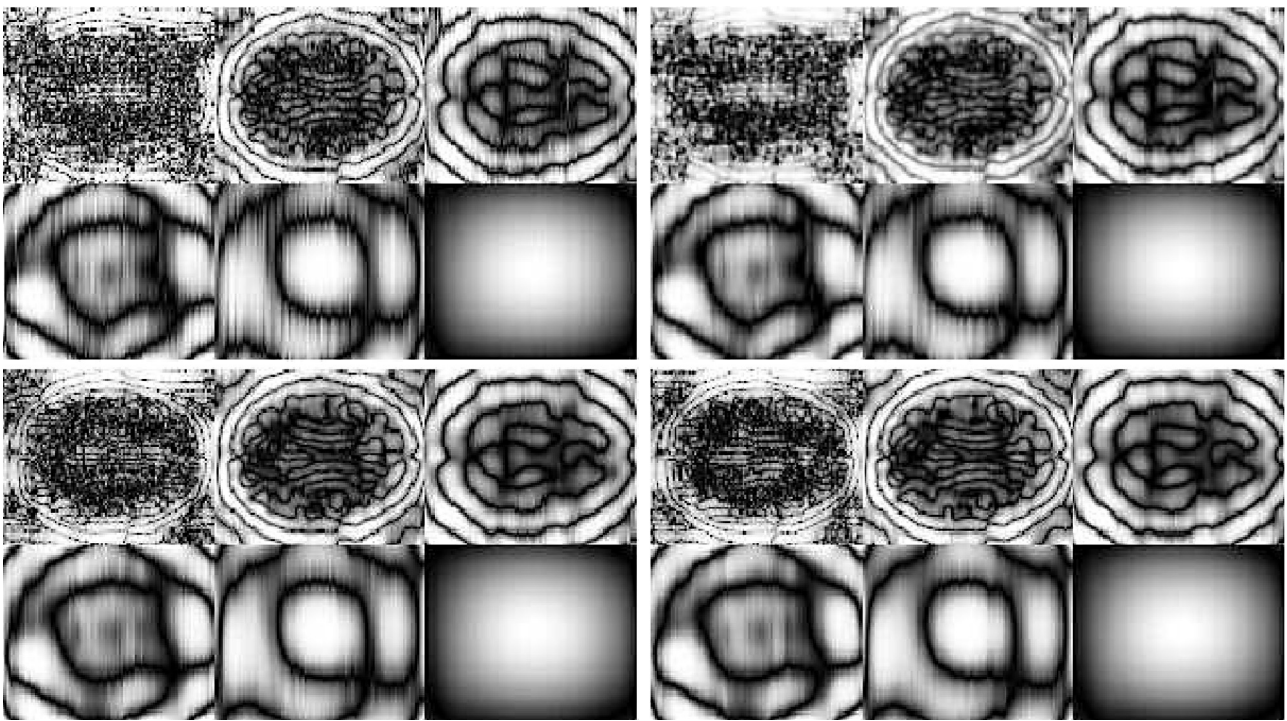
Fig. 4. 2DEEMD with spatial smoothing and an added noise level of $a_n = 0.2\sigma$: *Top left*: Ensemble size $N_E = 20$, *Top right*: Ensemble size $N_E = 20$, Gaussian filtering, *Bottom left*: $N_E = 100$, *Bottom right*: $N_E = 200$.

quality and computational costs, we fixed the number of sifting steps to this suggested number in our study.

4.1.2. Ensemble size

A large number of members forming an ensemble, henceforth called *ensemble size* N_E, results in high quality decompositions as, due to self-averaging, the noise in the data becomes almost perfectly canceled out. But this strategy also results in a heavy computational load which often becomes prohibitive. Fig 4 shows the effect upon the BIMFs of varying the number of the members of an ensemble. Especially BIMF4 and BIMF5 when decomposed with a small number of members of the ensemble, show decomposition artifacts like the vertical lines visible in the images. Accordingly, in a large scale simulation, the number N_E of members comprising an ensemble has been varied systematically. As the ensemble size increases, these artifacts almost vanish. They rather disappear when the number of members of the ensemble exceeds $N_E \geq 100$. It can be seen that there is not much difference between an ensemble size of $N_E = 100$ and $N_E = 200$ members, respectively. However, the computational load increases linearly with he number of members forming an ensemble. Hence, an 2DEEMD with $N_E = 100$ members takes five times more computation time than an 2DEEMD with $N_E = 20$ members. Thus keeping computational costs low and still keeping image modes free from artifacts, we suggest applying a linear filter in combination with an 2DEEMD (2DEEMD-LF). 2DEEMD-LF works simply by applying a linear Gaussian filter which replaces each voxel in a BIMF with a Gaussian weighted average intensity in a 5×5 neighborhood of voxels around each voxel. As a result, this spatial smoothing almost eliminates all artifacts from the BIMFs. In Fig. 4 one can see clearly the effect of this smoothing filter. Consequently, in this work an ensemble size $N_E = 20$ with spatial smoothing to the activity distributions is used.

4.1.3. Noise amplitude

A clear effect on the quality of BIMFs is seen after changing the amplitude of the added noise. Fig 5 clearly demonstrates that with increasing noise amplitude mainly streak artifacts become very prominent. This is because the size of the ensemble is kept constant rather than increased with increasing noise added. This is enforced by the prohibitive computational load otherwise. As a consequence, in this study only a small noise amplitude of $a_n = 0.2 \cdot \sigma$, where σ denotes the standard deviation of the intensity distribution of the original fMRI images, has been chosen.

4.1.4. Number of image modes

Finally, in order to assure comparable results, the number of extracted BIMFs needs to be kept constant throughout this study. Fig. 6 shows that an optimal number of extracted BIMFs turned out to be $K = 6$. With seven or eight extracted BIMFs no further textures at larger spatial scales appeared. On the other hand, with less than $K < 6$ BIMFs, one can see that the last component does not represent a trend yet.

4.2. Classification

Visual inspection of the figures illustrating the differences between both conditions of the resulting BIMFs and VIMFs of a 2DEEMD analysis reveals clues as to whether and where differences in activations appear according to the two stimulus conditions applied. Such observations may be quantified by evaluating the performance of properly trained classifiers which provide adequate means to corroborate whether or not the textures making up the extracted image modes (BIMFs or VIMFs) contain discriminating differential activity distributions allowing for a robust classification of these features.

Classification algorithms operate by dividing a high-dimensional space into regions corresponding to different classes of data. For this application, the two classes considered are *(contour, non-contour) C = CT, NCT*. For each class, an activity distribution of a whole brain volume $\langle V(x, y, z) \rangle$ is computed which corresponds to an average over all trials for any of the two stimulus/response conditions. These data volumes are either concatenated into column vectors, or a 2DEEMD is applied to them to extract related volume modes *VIMF1–VIMF6*. Each of
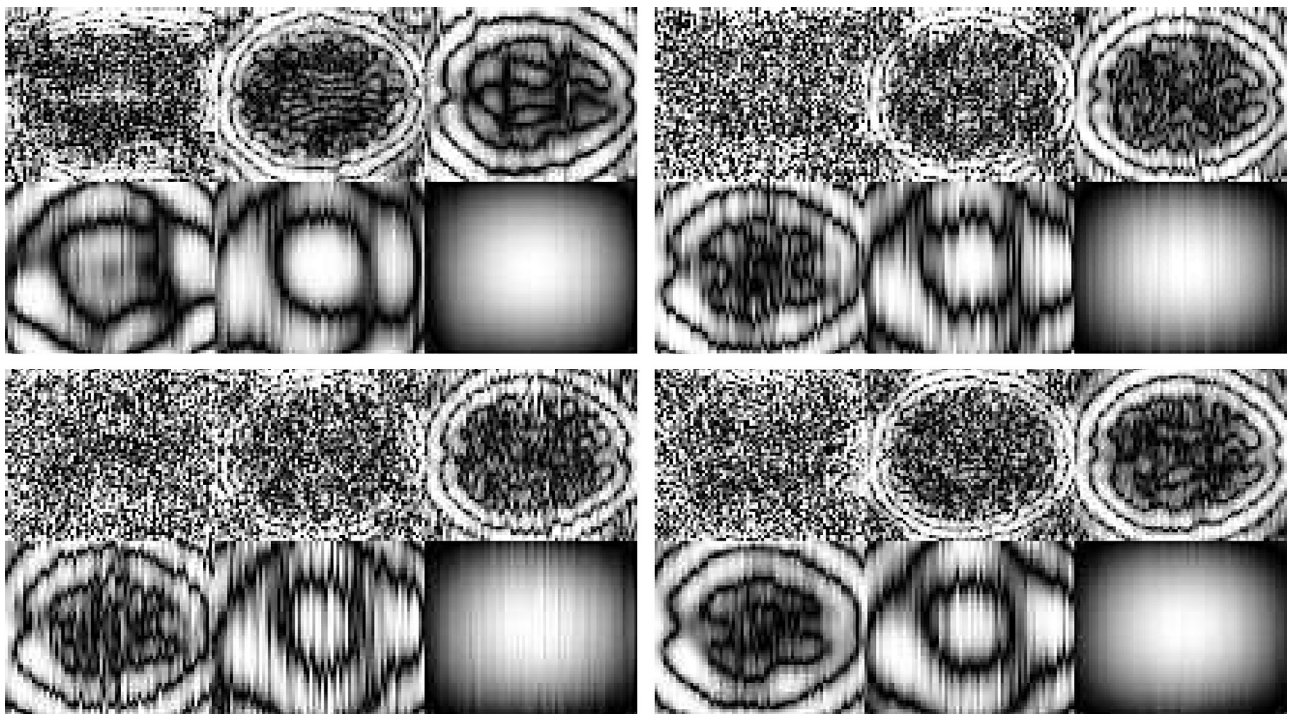
Fig. 5. 2DEEMD modes with noise added or ensemble size increased: *Top left*: $N_E = 20$, $a_n = 0.2\sigma$, *Top right*: $N_E = 20$, $a_n = 1.5\sigma$, *Bottom left*: $N_E = 20$, $a_n = 2.5\sigma$, *Bottom right*: $N_E = 100$, $a_n = 2.5\sigma$.

the latter also becomes concatenated into a column vector **m** for further processing. All such data vectors comprise many components rendering them impractical as input to a classifier. Hence, the high-dimensional textures need to be transformed into low-dimensional features proper for classification.

4.2.1. Feature generation

Given the high dimensionality of the data sets collected from only few subjects some dimensionality reduction is needed to cope with the small S, large R problem where S is the number of instances and R is the number of parameters. Features will be generated by decomposing either the raw data or the VIMFs, resulting from an 2DEEMD analysis, with either principal or independent component analysis. Dimension reduction can be achieved by applying a Principal Component Analysis (PCA). To perform a PCA, VIMFs from all $N_{sj} = 19$ subjects and for the two conditions, CT and NCT, studied are collected into a data matrix

$$\mathbf{M} = \begin{pmatrix} m_{11} & \dots & m_{1S} \\ m_{21} & \dots & m_{2S} \\ \vdots & \ddots & \vdots \\ m_{R1} & \dots & m_{RS} \end{pmatrix} \tag{13}$$
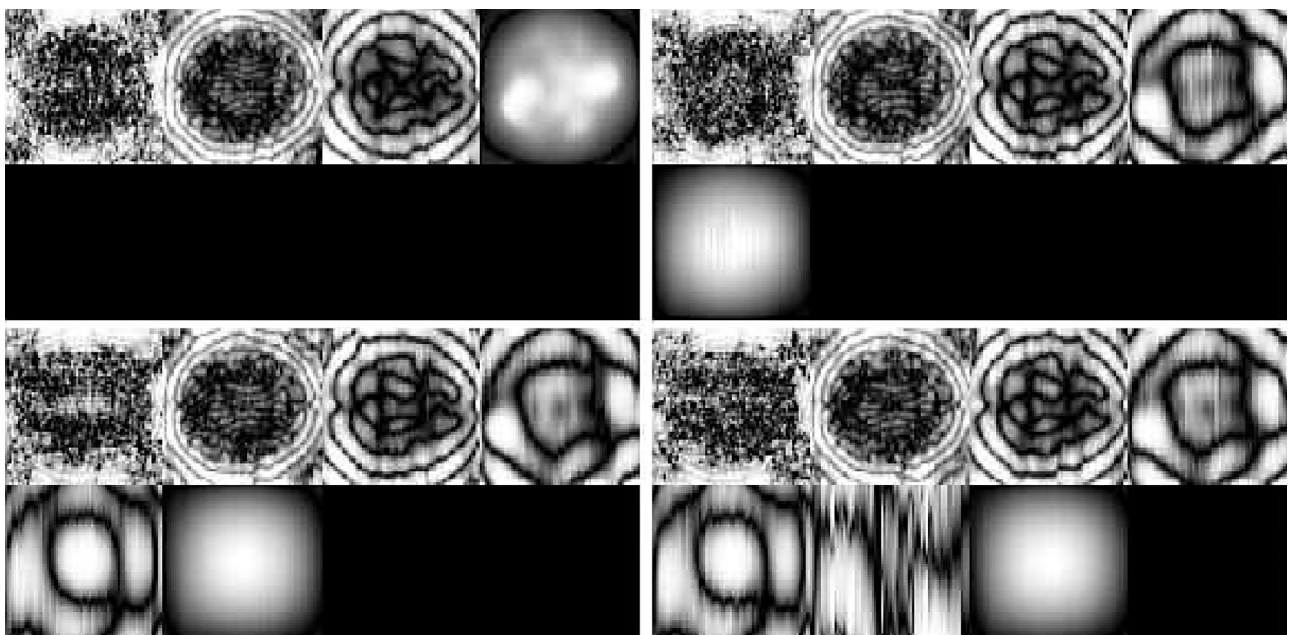

Fig. 6. 2DEEMD with variable number K of modes extracted. From *Top left* to *Bottom right*: $K = 4, 5, 6, 7$.

Then VIMFs can be projected onto eigenvolumes resulting from a PCA and the resulting projections are used as appropriate features for classification. The goal of a principal component decomposition of the VIMFs, obtained through a 2DEEMD, is to compute the eigenvolumes $\mathbf{U}$ of the co-variance or correlation matrix $\mathbf{R}$ that span the space of all voxels. This allows for a new representation of the data in an orthogonal axis system which maximizes the variance of the data along each principal direction. Projecting all VIMFs onto these eigenvector directions reveals the contribution of each eigenvector to the volume mode. PCA eigenvolumes can be determined by decomposing the $R \times S$ dimensional matrix $\mathbf{M}$ of VIMFs with the help of a *singular value decomposition* (SVD)

$$\mathbf{M} = \mathbf{UDV}^T \tag{14}$$

where, D is a diagonal matrix with $\min(R, S)$ non-zero *singular values* and $\mathbf{U}$ and $\mathbf{V}$ are the eigenvector matrices of the non-normalized correlation matrix $\mathbf{R} = \mathbf{MM}^T$ and the related kernel matrix $\mathbf{K} = \mathbf{M}^T\mathbf{M}$, respectively, whose corresponding column vectors $\mathbf{u}$, $\mathbf{v}$ form orthogonal eigenvectors in spaces of dimension $R \times R$ and $S \times S$, respectively.

Therefore the columns of $\mathbf{U}$ span the voxel space while the columns of $\mathbf{V}$ span the (participants $\times$ conditions) space. It is important to note that from only $S \ll R$ observations the components of the eigenvector matrix $\mathbf{U}$ cannot be determined reliably. Hence one has to resort to study the related kernel matrix as only an eigenvalue decomposition of matrix $\mathbf{K}$ is feasible. This finally yields, substituting results from above, for the *singular value decomposition* of the matrix of observations $\mathbf{M}$ the following relation

$$\mathbf{K} = \mathbf{M}^T\mathbf{M} = (\mathbf{UDV}^T)^T\mathbf{UDV}^T = (\mathbf{VDU}^T)\mathbf{UDV}^T = \mathbf{VD}^2\mathbf{V}^T = \mathbf{V\Lambda V}^T \tag{15}$$

Therefore the eigenvalues λ_s are the square of the singular values d_s and the eigenvector matrix $\mathbf{V}$ is the right eigenvector matrix of SVD. Hence, $\mathbf{\Lambda} = \mathbf{D}^2$ and the eigenvector matrix $\mathbf{U}$ of the correlation matrix $\mathbf{R}$ can be obtained from the matrix of observations $\mathbf{M}$ and its SVD via $\mathbf{U} = \mathbf{MV\Lambda}^{-1/2}$.

Now consider projecting all data vectors onto the new basis vectors, i.e. consider the projections $\mathbf{Z} := \mathbf{U}^T\mathbf{M}$. Hence $\mathbf{Z}$ represents the matrix of projections of the data vectors $\mathbf{M}$ onto the eigenvectors $\mathbf{U}$ of the correlation matrix $\mathbf{R}$ which also span the space of all voxels of the component images. From the discussion above it follows that

$$\mathbf{U}^T\mathbf{M} := \mathbf{Z} = \mathbf{DV}^T = \mathbf{\Lambda}^{1/2}\mathbf{V}^T \tag{16}$$

Note that both, $\mathbf{D}$ and $\mathbf{V}$ follow from an eigendecomposition of the kernel matrix of the observations. Every *row* $\mathbf{Z}_{n,*}$ of the projection matrix $\mathbf{Z}$ contains a projection of a data vector onto one of the new basis vectors $\mathbf{U}_{*,n}$. The latter are ordered via their corresponding eigenvalues $d_s = \sqrt{\lambda_s}$.

Independent components are achieved by applying a, yet to be determined, $S \times S$ rotation matrix $\mathbf{W}$ to the projected data $\mathbf{Z}$. The *INFOMAX* algorithm [12] was used to estimate the rotation matrix, and the new representation of the projected data is obtained via

$$\mathbf{S} = \mathbf{WZ} = \mathbf{WU}^T\mathbf{M} \tag{17}$$

Afterwards the rows of $\mathbf{S}$ are re-ordered according to their correlations to the rows of $\mathbf{Z}$. Therefore after re-ordering, the first row of $\mathbf{S}$ should have the largest correlation with the first row of $\mathbf{Z}$, the second row of $\mathbf{S}$ should have the largest correlation with the second row of $\mathbf{Z}$ and so on.

This allows to select only the most informative projections to be used as features for a classifier, for example. Anyway, only $S \ll R$ projections can be obtained which renders the problem tractable.

In summary, the eigenvalue decomposition of the kernel matrix $\mathbf{K}$, i.e. the matrix of inner products of the data vectors, provides all ingredients to compute the projections onto at most S directions. Each row of $\mathbf{Z}$ contains a projection onto one such basis vector. Again note that the latter are ordered via their corresponding eigenvalues λ_s. Considering the data set studied, a further dimension reduction is possible by selecting a subset of those S projections, e.g. choosing the $L < S$ leading rows of the projection matrix $\mathbf{Z}$. Concerning the independent projections $\mathbf{S}$, a similar dimension reduction can be achieved but the selected L independent projections are linear combinations of all orthogonal projections $\mathbf{Z}$. These independent projections do not obey any natural ordering principle, but the re-ordering step allows to align the projections according to the variance of the data.

Then the classifier will only have $L \leq S$ inputs and S examples which represents a stable situation in the sense that sufficient information is provided to the classifier to achieve a reliable classification of the data.

4.2.2. Support vector machine classifier

For classification, a soft margin SVM classifier, more specifically the C – SVM [9] algorithm as contained in the MATLAB Statistics Toolbox [40], has been used. The parameter C allows controlling the number of margin errors and support vectors. The optimization problem can be written in its dual form as (cf. [56]):

$$\underset{\boldsymbol{\alpha} \in \mathbb{R}^m}{\text{maximize}} \quad W(\boldsymbol{\alpha}) = \sum_{i=1}^{S-1} \alpha_i - \frac{1}{2}\sum_{i,j=1}^{S-1} \alpha_i \alpha_j y_i y_j k(\mathbf{z}_{(i)}, \mathbf{z}_{(j)}) \tag{18}$$

subject to $\quad 0 \leq \alpha_i \leq C \quad$ for all $i = 1, \ldots, S-1 \tag{19}$

and

$$\sum_{i=1}^{S-1} \alpha_i y_i = 0. \tag{20}$$

where $k(\mathbf{z}_{(i)}, \mathbf{z}_{(j)})$ represents the kernel dot product between the non-linearly mapped training data.

The mapping is represented by a sigmoidal kernel,

$$k(\mathbf{z}_{(i)}, \mathbf{z}_{(j)}) = \tanh(\gamma \mathbf{z}_{(i)}^T \mathbf{z}_{(j)} + r) \tag{21}$$

with parameters $\gamma > 0$, $r < 0$. These parameters represent user-defined parameters to be assigned before running the optimization algorithm. The outcome of the optimization are the Lagrangian values, $0 \leq \alpha_i \leq C$. The training examples, known as support vectors, are related with the non-zero Lagrangian coefficients. Cross-validation is effected by a leave-one-out technique where every data vector is once used for testing.

The resulting decision function, considering a test vector $\mathbf{z}_{test}$ to be classified takes the form

$$f(\mathbf{z}_{test}) = \text{sgn}\left(\sum_{i=1}^{S-1} \alpha_i y_i k(\mathbf{z}_{test}, \mathbf{z}_{(i)}) + b\right) \tag{22}$$

where b denotes the distance of the hyperplane from the origin. Note that only the training examples $\mathbf{z}_{(i)}$ with $\alpha_i \neq 0$ (support vectors) need to be available for testing.

4.2.3. Random forest classifier

The random forest algorithm, developed by Breiman [7], is a set of binary decision trees, each performing a classification. The final decision is taken by majority voting. Each tree is grown using a bootstrap sample from the original data set. Each node of the tree randomly selects a small subset of features for splitting the data into two subsets. An optimal split separates the set of samples at each node into two supposedly more homogeneous or pure sub-groups

with respect to the class of its elements. The impurity level of each set of samples with respect to class membership can be measured by the *Gini index*. Denoting this class labels by ω_c, $c = 1 \ldots C$, the Gini index of node i is defined as

$$G(i) = 1 - \sum_{c=1}^{C} (P(\omega_c))^2$$

where $P(\omega_c)$ is the probability of class ω_c in the set of instances that belong to node i. Note that $G(i) = 0$ whenever node i is pure, e.g. if its data set contains only instances of one class. To perform a split, one feature z_l is tested on the set of samples with n elements according to $z_l > z_{th}$, which is then divided into two sub-groups (left and right) with n_l and n_r elements. The change in impurity is computed as

$$\Delta G(i) = G(i) - \left(\frac{n_l}{n} G(i_l) + \frac{n_r}{n} G(i_r) \right)$$

That feature among all z_l and the threshold z_{th} which yield the largest decrease of the Gini index is chosen to perform the split at node i. Each tree is grown independently, and no pruning is applied on the grown trees. The main steps of this algorithm [25,24] are the following:

1. Given a data set $\mathcal{T}$ with N examples, each with L features, select the number T of trees, the dimension of the subset $mtry < L$ of features, and the parameter that controls the size of the tree (it can be the maximum depth of the tree, the minimum size of the subset in a node to perform a split).
2. Construct the $t = 1 \ldots T$ trees.
   (a) Create a training set $\mathcal{T}_t$ with N examples by sampling with replacement the original data set. The out-of-bag data set $\mathcal{O}_t$ is formed with the remaining examples of $\mathcal{T}$ not belonging to $\mathcal{T}_t$.
   (b) Perform the split of node i by testing one of the $mtry = \lfloor \sqrt{L} \rfloor$ randomly selected features.
   (c) Repeat step 2b up to the tree t is complete.
   (d) Use the out-of-bag (OoB) data $\mathcal{O}_t$ as test set of the t tree. Keep track of the votes for each class instances each time they are in out-bag data sets. The number of false classifications averaged over all cases yields the OoB error estimate. In this way an out-of-bag (OoB) error results measuring the classification performance of the RF classifier.
3. Repeat step 2 to grow next tree if $t \neq T$. In this work $T = 500$ decision trees were employed.

After training, the importance of each feature z_l in the ensemble of trees can be computed by adding up the values of $\Delta G(i)$ of all nodes i where the feature z_l is used to perform a split. Then it is possible to identify the relative importance of the features.

5. Results

5.1. Resulting volume modes

Note that the analysis of the fMRI experiments focusses onto the two stimulus/response conditions, i.e. *contour true* (CT) and *non-contour true* (NCT). Hence, results will be discussed later on in terms of differences of normalized VIMFs for both conditions. Altogether VIMFs from 19 subjects and for two stimulus conditions have been obtained as an average over N_t trials during the three sessions, resulting in a total of 38 VIMFk for each k. The activity distributions within the VIMFs have been normalized for both conditions taken together. Results are presented as difference images

$$\Delta VIMFk = VIMFk_{CT} - VIMFk_{NCT} \qquad (23)$$

Table 1
MNI coordinates of the activity distributions highlighted in Figs. 7 and 8.

Modes	x	y	z	Anatomical structure
VIMF1	−63	−16	10	Left superior temporal gyrus
	−63	−22	16	Left postcentral gyrus
	−69	−31	4	Left middle temporal gyrus
	60	−43	−5	Right middle temporal gyrus
VIMF2	0	44	−17	Left rectal gyrus
VIMF3	−48	8	−35	Left inferior temporal gyrus
	−48	5	−29	Left middle temporal gyrus
	57	−46	−14	Right inferior temporal gyrus
	−45	2	−14	Left superior temporal gyrus
	−42	11	−17	Left temporal pole
	42	8	−38	Right medial temporal pole
	54	−22	−20	Right inferior temporal gyrus
VIMF4	−18	−85	4	Left superior occipital gyrus
	−30	−70	−17	Left fusiform gyrus
	0	−13	70	Left paracentral lobule
	−3	32	−17	Left rectal gyrus
VIMF5	0	44	40	Left superior medial gyrus
	−60	−52	−2	Left medial temporal gyrus
	0	32	61	Left superior medial gyrus
	63	−46	−2	Right middle temporal gyrus
SPM1	45	−25	64	Right postcentral gyrus
	36	−19	70	Right precentral gyrus
	−42	−22	64	Left precentral gyrus
SPM2	0	50	1	Left anterior cingulate cortex
	0	32	58	Left superior medial gyrus
	−36	−13	67	Left precentral gyrus
	51	20	−11	Right inferior frontal gyrus
	30	8	−20	Right temporal pole
	−6	2	10	Left caudate nucleus

which have been normalized separately to clearly show the, sometimes small, differences. Only differences above $0.7\Delta_{max}$ are shown in the images which exhibit an axial, a sagittal and a coronal view. In general, a high biological variability is observed as seen in the figure for *VIMF*3 which is provided as supplementary material. However, across all 19 subjects activity is consistently localized in the area of the temporal gyrus, though to a varying extent. For visualization purposes, the MRIcro analyze viewer [54] has been used.

Fig. 7 illustrates differences $\Delta VIMFk$, $k = 1, \ldots, K$ as averages over all subjects to highlight robustly obtained activation loci. The differences corresponding to $k = 2$ to $k = 4$ clearly show highly focused and spatially localized activities. $\Delta VIMF2$ exhibits activity almost exclusively in the left rectal gyrus. $\Delta VIMF3$, instead, shows activity mainly in the temporal gyrus, but activity is more pronounced in the left temporal gyrus compared to the right temporal gyrus, especially in the left inferior and middle temporal gyrus. $\Delta VIMF4$, finally, exhibits a pronounced activity in the (left) paracentral lobule. Note that the activity distribution in each difference image has been normalized separately to the range 0–1 and only the highest 30% of the activities are shown in the images, overlaid onto an anatomical image. Corresponding MNI coordinates of these localized activity blobs are collected in Table 1.

Considering a comparative analysis of the activity distributions resulting from a 2DEEMD analysis with the ones obtained using the canonical SPM tool, Fig. 8 clearly demonstrates the superior detail and spatial localization which $\Delta VIMF2$, $\Delta VIMF3$ and $\Delta VIMF4$ exhibit compared to the SPM results which most closely resembles $\Delta VIMF4$ on a first level analysis, denoted SPM1. Only at a second level of analysis, denoted SPM2, also other activity blobs become visible, though less localized and focused. Note that only activations corresponding to the same level of statistical significance are exhibited to render images from both approaches comparable.
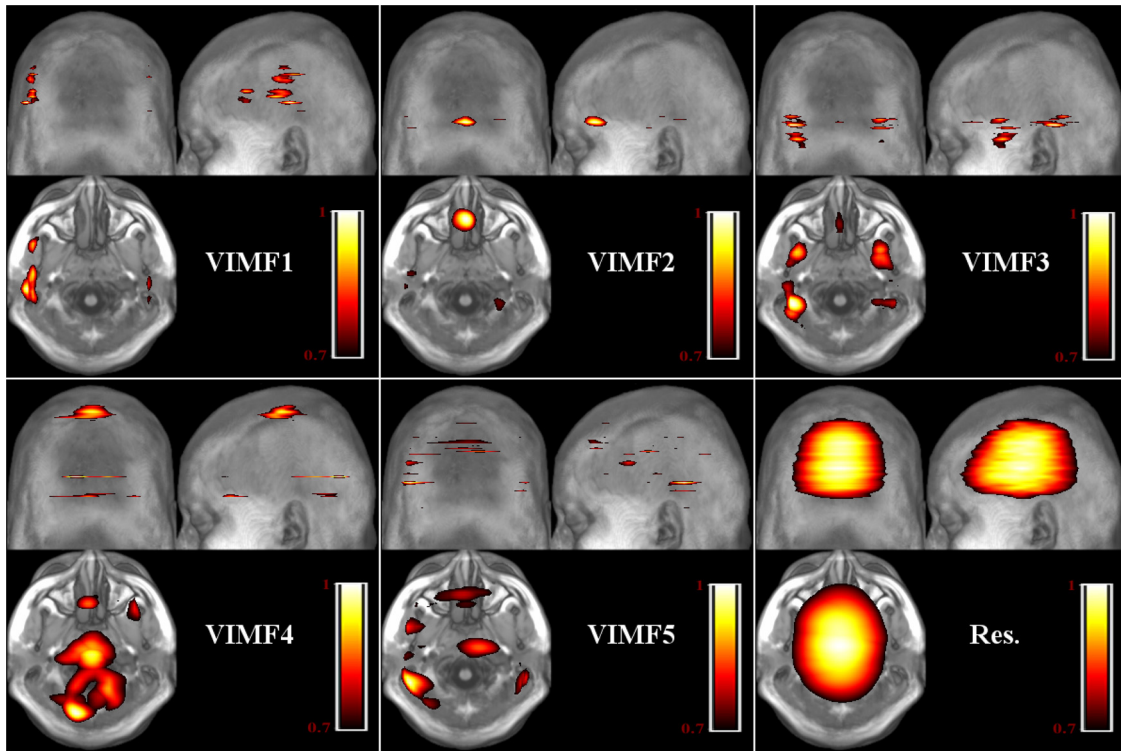
Fig. 7. Illustration of the six difference VIMFs resulting from an 2DEEMD decomposition of a whole brain volume. The difference refers to the VIMFs for the two conditions CT and NCT, respectively. Each difference VIMF is normalized separately to enhance visibility.

5.2. Classification results

For classification either orthogonal and independent projections are the inputs of the classifiers. Considering orthogonal projections, the following two data sets have been considered:

- Projections onto principal directions of average volumes $\langle V_{sc}(x, y, z)\rangle$ deduced from "raw" data and collected in an $L \times S$ matrix $\mathbf{Z}_{av}$.
- Projections onto principal directions of volume modes $VIMFk$, $k = 1, \ldots, K$ deduced from a 2DEEMD decomposition of average volumes $\langle V(x, y, z)\rangle$ and collected in an $L \times S$ matrix $\mathbf{Z}_{vm}$.

These projections are called orthogonal projections and are used as features for classification. The scree plot, see Fig. 9, illustrates the normalized eigenvalue spectrum and related cumulative sum of variances for the most discriminative volume mode $VIMF3$. It can be seen that the eigenvalue spectrum levels off after only $L = 10$ eigenvalues which in total already explain roughly 80% of the data variance. The eigenvolumes, i.e. the columns of matrix $\mathbf{U}$, represent uncorrelated partial activity distribution in brain. Fig. 10 illustrates the eigenvolume related with the second largest eigenvalue for both the raw data and VIMF3, respectively. Both underline the relevance of the occipital area for contour integration. However, the activity distribution provided by VIMF3 is much more focused than in case of the raw data.

Given all orthogonal projections $\mathbf{Z}$ discussed above, a rotation matrix $\mathbf{W}$ is estimated. The resulting independent projections, after re-ordering, are collected

- in an $L \times S$ matrix $\mathbf{S}_{av}$ in case of the projected "raw" data, or
- in an $L \times S$ matrix $\mathbf{S}_{vm}$ in case of the projected volume modes.

The orthogonal or independent projections thus obtained have been input to either an SVM or an RF classifier. Both RF and SVM training represent stochastic algorithms. SVM training can

be performed efficiently by applying a sequential minimization optimization (SMO) technique which breaks the large quadratic programming (QP) problem into a sequence of smaller QP sub-problems which can be solved analytically [56]. For both classifiers, training and testing was repeated 10 times while permuting the whole data set randomly, and a leave-one-out cross-validation (LOOCV) strategy was invoked to obtain reliable results. Several metrics were used to measure the performance of the classifiers, namely accuracy (acc), sensitivity (sens), specificity (spec) and the receiver operating characteristic (ROC) curve.

5.2.1. Raw data

First "raw" features, i.e. the projections $\mathbf{Z}_{av}$ of average volumes resulting from "raw" data onto their principal directions, have been fed to an SVM classifier yielding an average accuracy $acc = 0.75 \pm 0.03$, an average specificity $spec = 0.72 \pm 0.03$ and an average sensitivity $sens = 0.77 \pm 0.05$ (see first column of Fig. 11). These figures have been obtained by varying the number of principal components L and choosing the optimal number of PCs ($L = 10$) according to the highest accuracy achieved.

Next, the same "raw" features have been fed to an RF classifier resulting in an average accuracy $acc = 0.66 \pm 0.04$, an average specificity $spec = 0.66 \pm 0.07$ and an average sensitivity $sens = 0.65 \pm 0.07$. These results has been obtained with the total number of features ($L = 38$) according to the highest accuracy obtained.

The orthogonal projections of the raw data onto the PCs leave some statistical dependencies, hence ICA was applied to remove the latter. The resulting independent projections $\mathbf{S}_{av}$ were again fed into the SVM classifier resulting in the following statistical measures: an average accuracy $acc = 0.64 \pm 0.02$, an average specificity $spec = 0.64 \pm 0.02$ and an average sensitivity $sens = 0.64 \pm 0.05$. Then, the same ICs features have been fed to a RF classifier getting an average accuracy $acc = 0.66 \pm 0.00$, an average specificality $spec = 0.68 \pm 0.00$ and an average sensitivity $sens = 0.63 \pm 0.00$
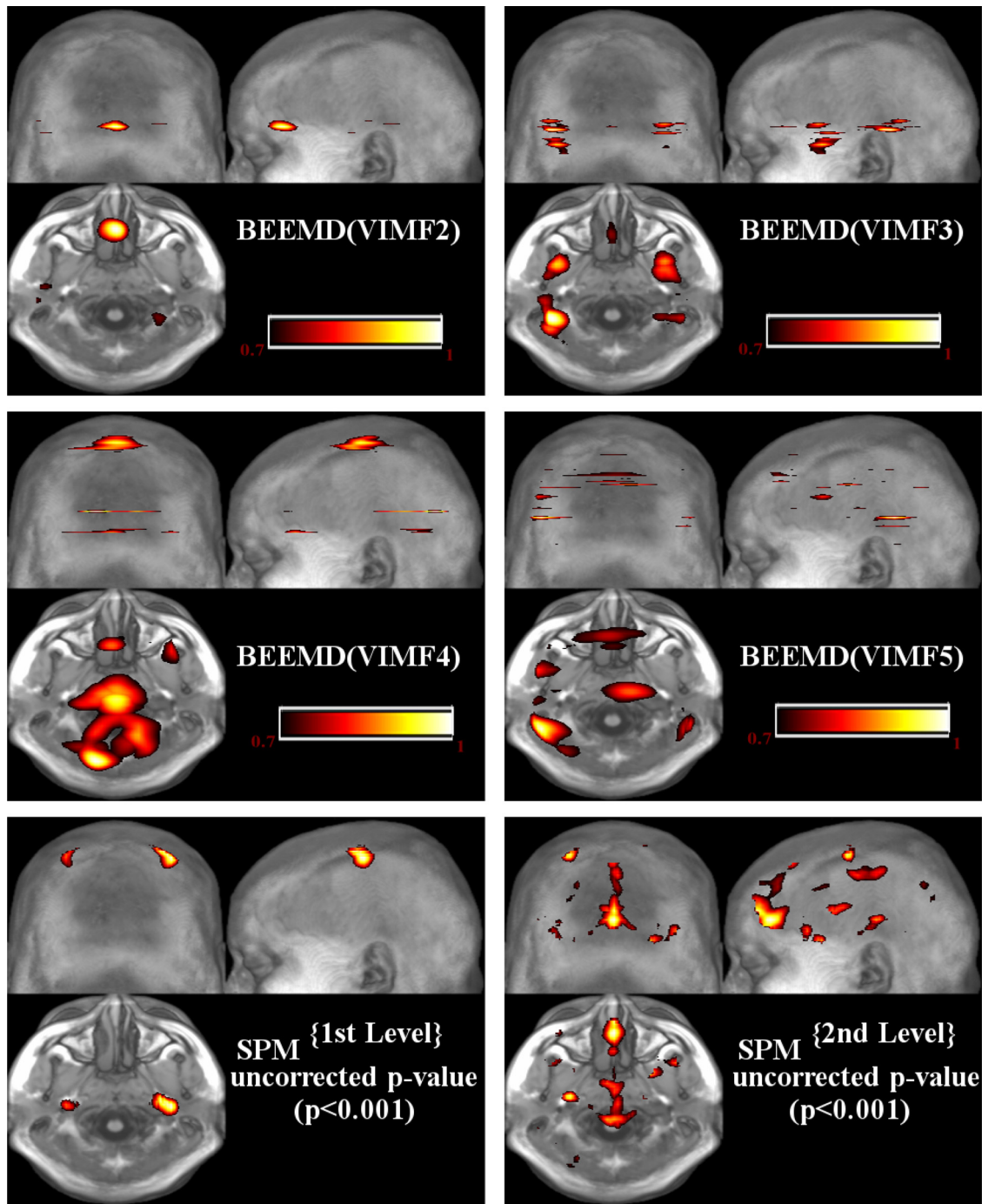
Fig. 8. Illustration of the difference maps of VIMF2, VIMF3 and VIMF4 compared to the SPM difference map. All difference maps are averages over all 19 subjects. The difference refers to the VIMFs for the two conditions CT and NCT, respectively.

5.2.2. Volume image modes

Obviously projections $\mathbf{Z}_{av}$ of "raw" data yield poor classification accuracies only. A 2DEEMD decomposition of the "raw" data set resulted in six volume modes $VIMFk$, $k = 1, \ldots, K = 6$ which might have been further processed by a Gaussian smoothing filter. Afterwards, the corresponding orthogonal ($\mathbf{Z}_{vm}$) or independent ($\mathbf{S}_{vm}$) projections of the VIMFs were used as appropriate features and have been fed into either an SVM or an RF classifier trained to differentiate the stimulus/response conditions CT and NCT.

An exhaustive experimental evaluation of the classifiers has been conducted, having as input either $\mathbf{Z}_{vm}$ or $\mathbf{S}_{vm}$. Here the number of features L was also a variable for the SVM classifier, but

kept constant to $L = 38$ in case of the RF classifier. The results show that the SVM presents the best performance with $L = 11 \pm 2$ input features. Furthermore, both classifiers exhibit their highest performance with features extracted from VIMF3. Even the remaining modes, with the exception of VIMF1, also present better results than the raw data in many cases. Moreover, the performance of the classifiers is better with orthogonal features than with independent features. And the linear filtering, applied to the VIMFs, also has a positive impact on the performances. Best results are summarized in Tables 2–5 provided in an.

Fig. 11 illustrates the accuracy achieved with all VIMFs resulting from an SVM classifier and Gaussian filtering (exp. 2). Fig. 12
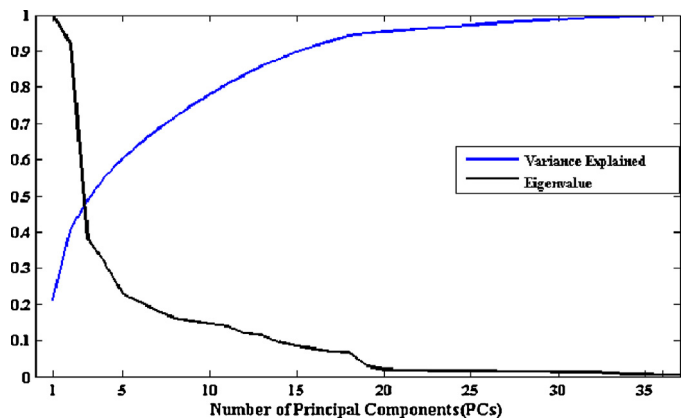
Fig. 9. Normalized eigenvalue spectrum and related cumulative variance for volume mode *VIMF*3 after decomposition with PCA.

provides a more complete picture. It illustrates the dependence of accuracy (acc), specificity (spec) and sensitivity (sens) on the number of PCs extracted, hence the dimension of the feature subspace. These statistical measures were achieved using features, i.e. projections, of the first $\mathbf{Z}_{VIMF1}$ and third $\mathbf{Z}_{VIMF3}$ volume modes, respectively. While *VIMF*1 mostly represents noise, *VIMF*3 exhibits textures which provide the most discriminative features for contour vs non-contour stimuli. As an additional statistical measure, Fig. 13 presents the related *receiver operating characteristic* (ROC) curves for all VIMFs and average volumes resulting from a data decomposition involving Gaussian filtering (exp. 2). The related area-under-curve (AUC) indicator yields $AUC = 0.86$ and $AUC = 0.80$ in case of *VIMF*3 classified with SVM and RF, respectively.

Corresponding measures in case of *VIMF*4 amount to $AUC = 0.82$ and $AUC = 0.78$, respectively.

6. Discussion

The data analysis presented in this study considers a decomposition, employing 2DEEMD, into intrinsic modes which represent textures on characteristic spatial scales of local variations in the neuronal activity distribution during a contour integration task. According to the EMD principle, the first intrinsic mode (VIMF1) represents textures with the highest spatial frequencies contained in the data, and subsequent modes represent textures with correspondingly lower spatial frequencies. Finally, the residual represents any spatially non-oscillating background activity. Proper features have been deduced from projecting these intrinsic modes onto their respective principal (PC) or independent (IC) components. These features finally have been fed into two classifiers, a SVM and a RF of decision trees. The aim of the classification was to corroborate the superior performance, with respect to the classifying "raw" data, of the deduced features in discriminating between the two stimulus conditions. Thereby classification also corroborates the decisive information content of the highest scoring modes with respect to the spatial distribution of neuronal activity when processing visual stimuli during contour integration. These modes highlight those brain areas which actively integrate oriented contrast edges into contours.

For grouping stimulus-related activity distributions, two classifiers were considered: a SVM, employing a sigmoidal kernel, and a RF of decision trees. With a kernel SVM, best classification performance was achieved constructing a feature vector with the first $L = 11 \pm 2$ projections (either orthogonal or independent) of the VIMFs. The eigenvalue spectrum indicates that the first $L = 11$
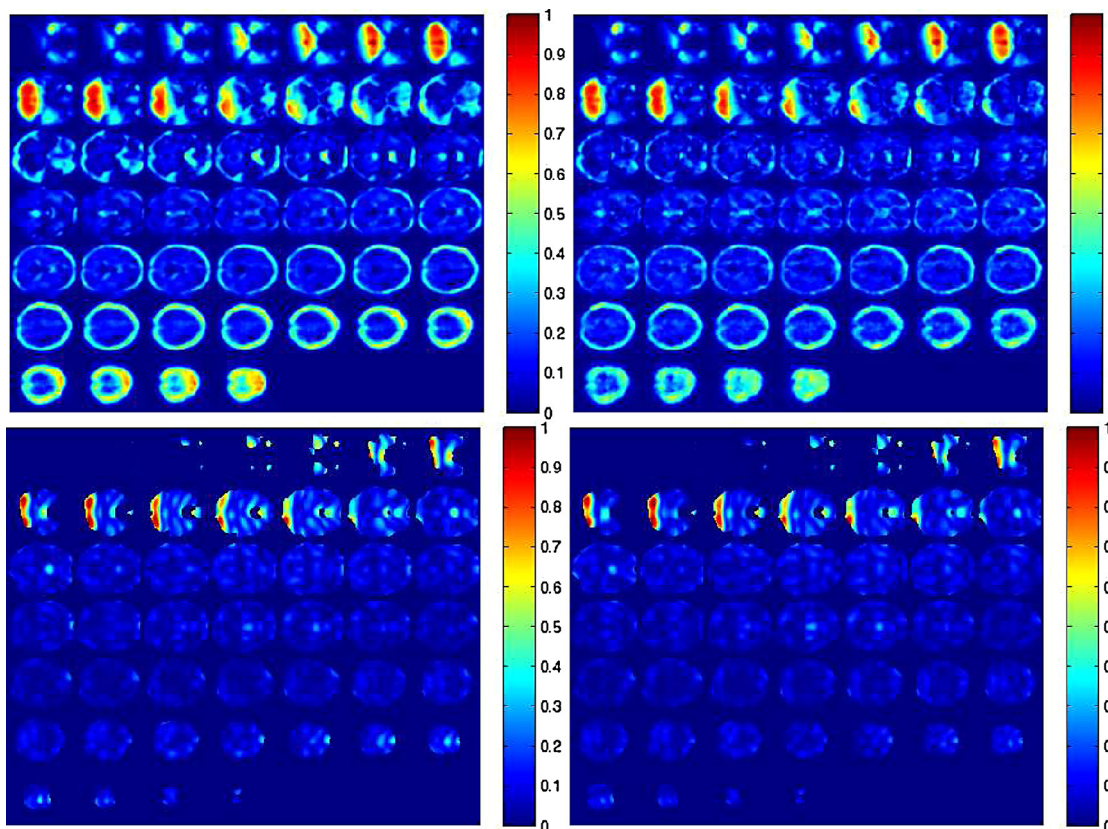

Fig. 10. *Top*: Illustration of the eigenvolume of the raw data obtained by PCA (*left*) and ICA (*right*) feature extraction. *Bottom*: Illustration of the eigenvolume of *VIMF*3 obtained by PCA (*left*) and ICA (*right*) feature extraction.
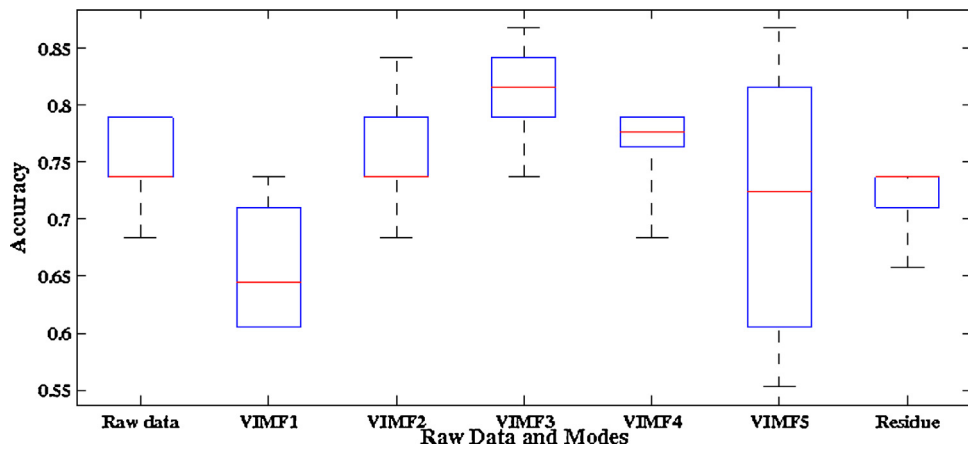
Fig. 11. Boxplot comparing the accuracy achieved by the SVM classifier using projections of the "raw" data as well as of the volume modes (VIMFs) resulting from a 2DEEMD analysis with subsequent Gaussian smoothing.
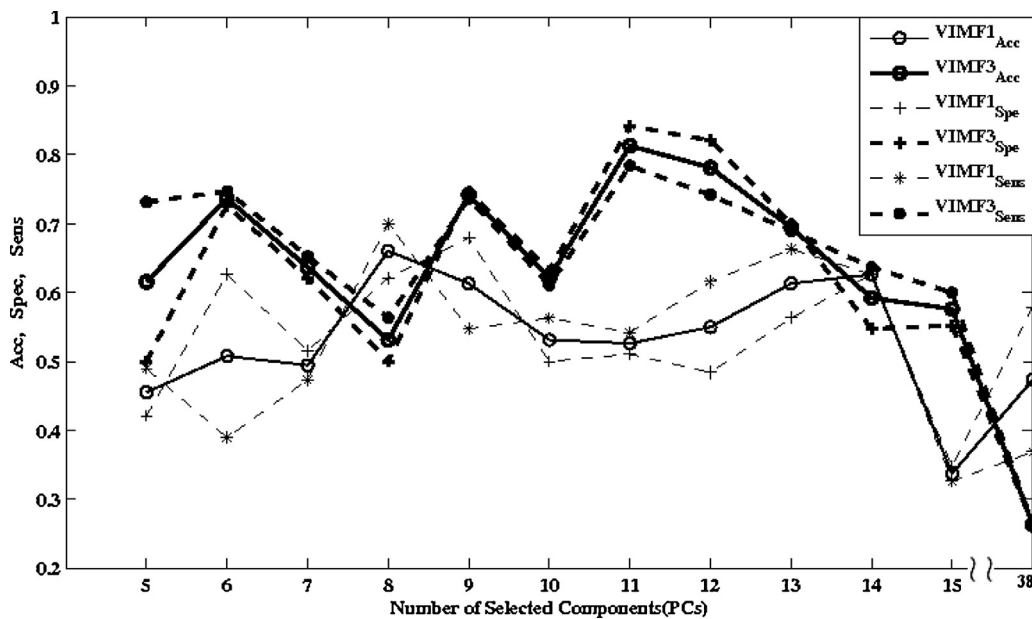

Fig. 12. Variation of statistical measures, obtained with SVM and Gaussian filtering, with the number of principal components extracted from volume modes *VIMF*3 and *VIMF*1, respectively.
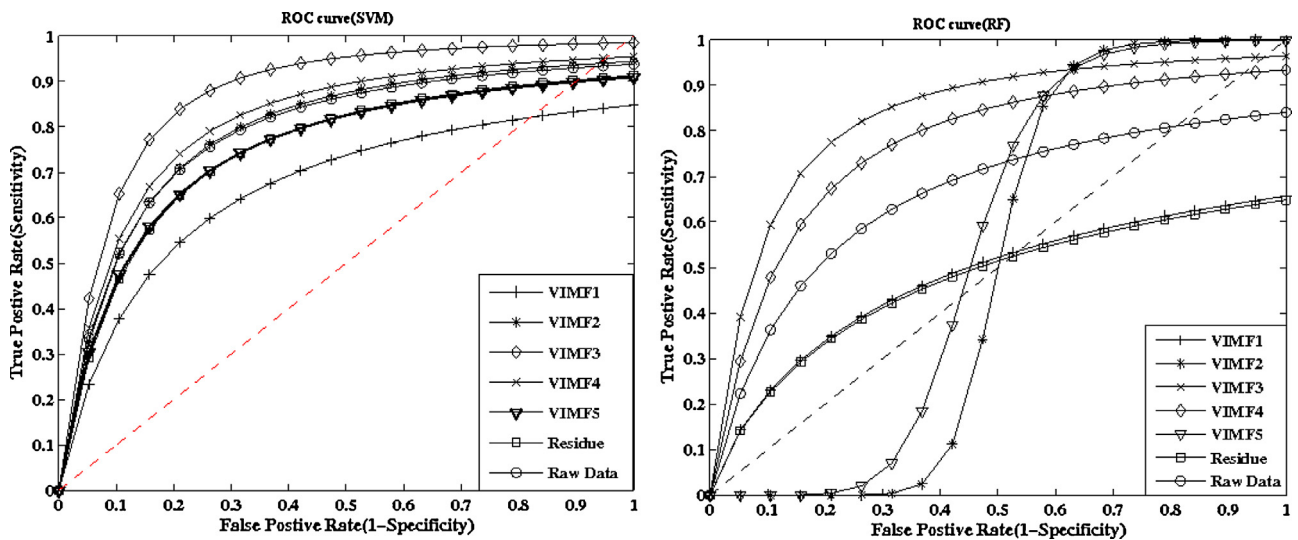

Fig. 13. Experiment 2 receiver operating characteristics (ROC) from all six volume modes (VIMFs). *Left*: ROC curves of VIMFs resulting from an SVM classification. *Right*: ROC curves of VIMFs resulting from an RF classification.
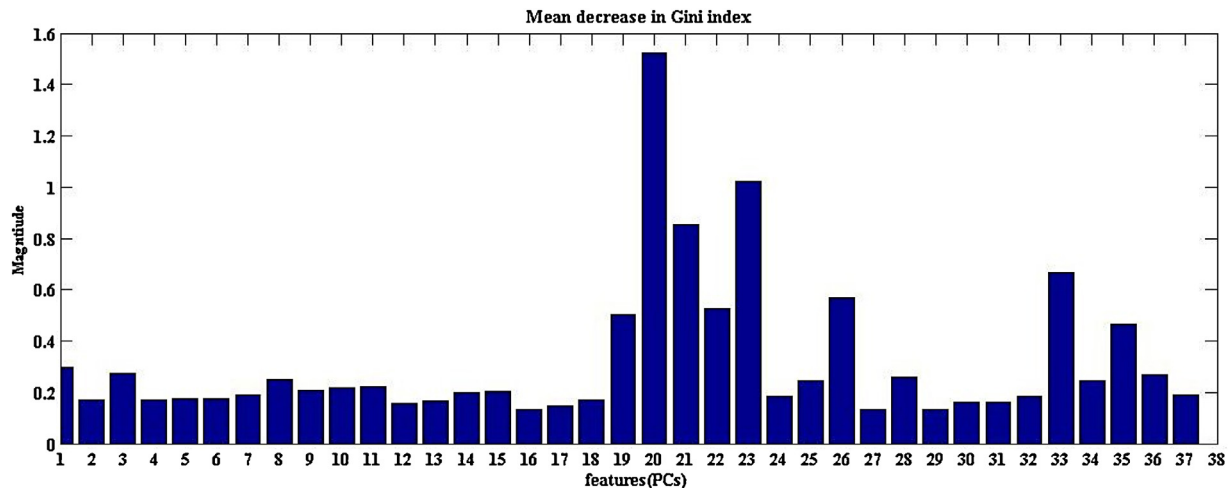
Fig. 14. The plot shows the Mean Decrease Gini Index for each feature (PCs) generated by PCA-RF applied to VIMF3.

PCs already explain roughly 90% of the variance of the data. They thus span a subspace of the data space which provides the relevant information for decision making of the classifier. Including further projections onto PCs with $L > 11$ decreases the accuracy achieved. This indicates that these projections provide distracting information to the SVM classifier. A RF of decision trees employs a random variable selection scheme. Good classification results are only obtained if all projections, i.e. all information being available, contribute to the decision making. In addition, the RF uses a bagging technique to improve classification predictions with unstable classification models. The RF algorithm also offers an easy way to measure the importance of any variable for decision making. Generally, two importance measures are discussed in literature: mean decrease accuracy and mean decrease Gini. The latter is reported to show greater robustness against small variations in the data, hence was chosen here. So, an RF classifier measures the importance of each feature on the decision process by using the Gini importance value. The latter is the sum (or the average) of the Gini index reduction over all nodes in which the specific feature is used to perform the split. Fig. 14 reveals that the Gini importance parameter exhibits a strong peak around features nr. 19–23 contrary to the SVM classifier which works better employing the first $L \approx 11$ components. In order to make a fair comparison between the two classifiers SVM and RF, leave-one-out cross-validation (LOOCV) is applied to both. The RF does cross-validation intrinsically by using a bagging technique. The out-of-bag (OoB) error normalized by the number of trees is reported in Fig. 15. It illustrates the general behavior of the running OoB-error when we train a random forest of 500 trees with $mtry = 6$ variables at each node. For *VIMF*3 and *VIMF*4, the OOB-error drops quickly to its minimal value $OoBerror \approx 0.27$ after ~200 trees for both *VIMF*3 and *VIMF*4. For the "raw" data, the OoB-error shows a much more moderate decline within ~200 trees and then levels off at $OoBerror \approx 0.40$. These results clearly show that the highest
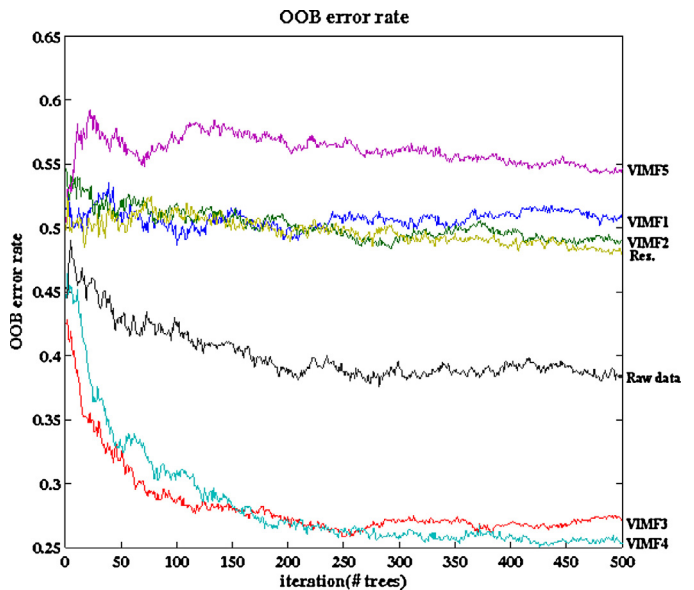

Fig. 15. Out-of-Bag (OoB) error rate from all six volume modes (VIMFs) resulting from an RF classifier using Gaussian filtering (exp. 2). The OoB curve for the raw data is shown for comparison, too.

accuracy is achieved with projections of *VIMF*3 consistently with both classifiers, SVM and RF, respectively, which both substantially outperform a direct classification of average volumes.

Gaussian filtering applied to the VIMFs before the feature generation stage improve results considerably. Thus Gaussian filtering obviously can deal with artifacts resulting from an EMD decomposition. This also helps to keep the number of ensembles, hence the

Table 2
Statistical measures evaluating classification results obtained by PCA and and SVM classifier either without (exp. 1) or with (exp. 2) applying a linear Gaussian filter to the VIMFs.

| SVM						
	Experiment 1			Experiment 2		
	Acc ± std	Spec ± std	Sens ± std	Acc ± std	Spec ± std	Sens ± std
VIMF1	0.72 ± 0.05	0.69 ± 0.06	0.75 ± 0.56	0.66 ± 0.05	0.62 ± 0.07	0.70 ± 0.07
VIMF2	0.79 ± 0.06	0.79 ± 0.04	0.78 ± 0.10	0.75 ± 0.05	0.75 ± 0.04	0.75 ± 0.09
VIMF3	**0.80 ± 0.05**	**0.82 ± 0.07**	**0.79 ± 0.05**	**0.81 ± 0.04**	**0.84 ± 0.04**	**0.78 ± 0.05**
VIMF4	0.79 ± 0.06	0.83 ± 0.08	0.75 ± 0.08	0.77 ± 0.03	0.75 ± 0.04	0.77 ± 0.05
VIMF5	0.74 ± 0.03	0.75 ± 0.04	0.72 ± 0.07	0.72 ± 0.11	0.66 ± 0.10	0.77 ± 0.14
Res	0.77 ± 0.03	0.74 ± 0.07	0.79 ± 0.04	0.72 ± 0.03	0.71 ± 0.07	0.73 ± 0.04
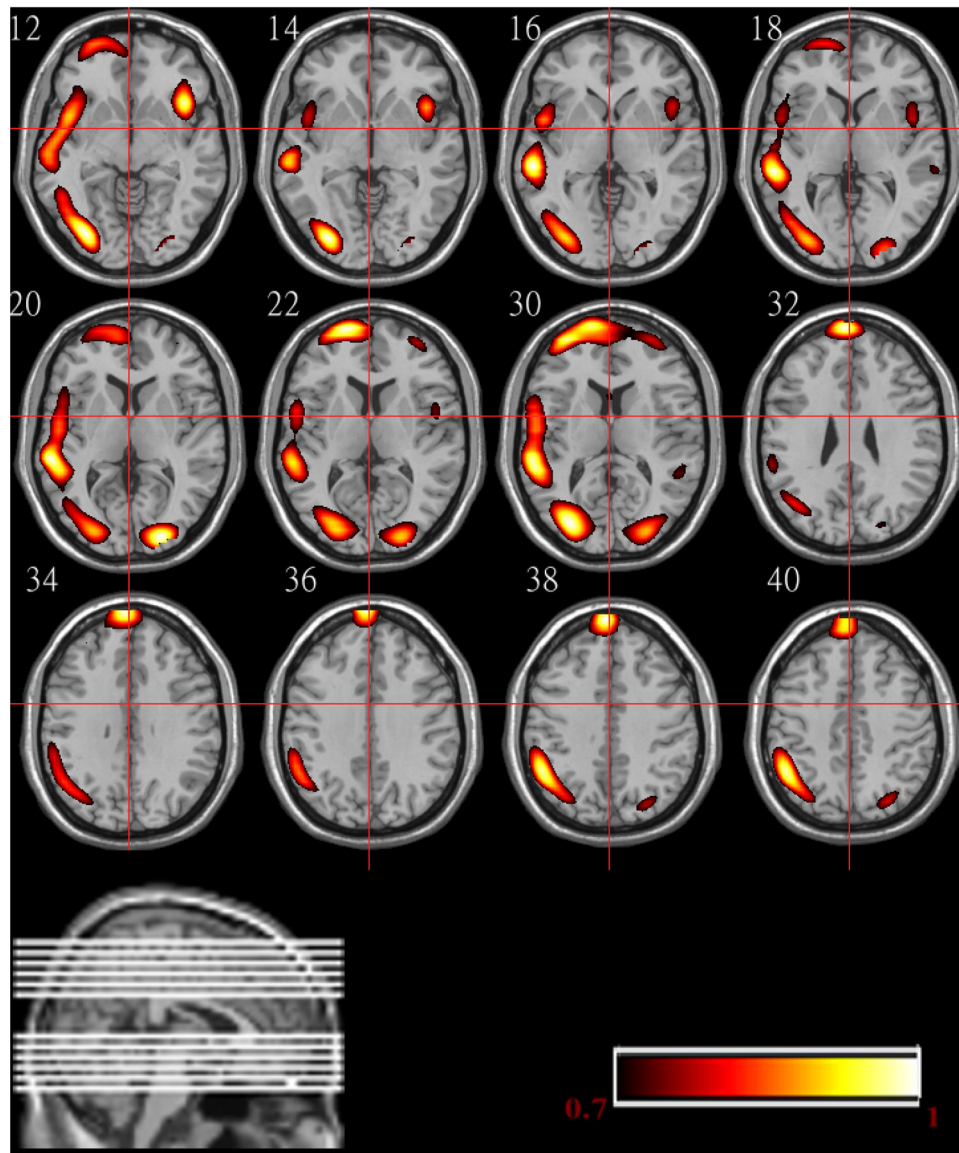
Fig. 16. Illustration of the activity distribution corresponding to *VIMF*3 overlaid to an anatomical image. The activity distribution corresponds to the response to a contour stimulus, denoted as "contour true" (CT).

computational load, conveniently small. With or without Gaussian linear filtering, the best discriminative power is observed with *VIMF*3. The latter can be visualized by overlaying the related activity distribution onto an anatomical image of a brain slice. Fig. 16 illustrates *VIMF*3 of one subject. For clarity of presentation, only 12 slices are shown. These slices are ordered from bottom to top as indicated by the position of the white lines on the axial brain slice. The highlighted brain regions are in good accordance with results of previous neuroimaging studies that typically revealed an increase of neural activity for contour compared to non-contour conditions within middle and lateral occipital areas [2,57]. Also, left frontal activity was indicative for the stimulus type in this subject. Most importantly, the results clearly demonstrate that contour integration involves higher brain areas also and is not confined to the visual cortex.

6.1. Relation to other works

In general, classification analysis tests hypotheses in terms of separating pairs (or more) of conditions. Note that the hypothesis is that a different pattern of activity occurs in the voxels making up a region, not that the activation level is different. This enables us to stay away from interpreting BOLD patterns in terms of activated voxels, a term which means that these neurons are active more than others, which may or may not be correct [15]. The type of hypothesis and associated test is especially useful if the conditions under investigation recruit different neural networks. We here used a visual detection task where spatially distributed Gabor patterns had to be grouped into continuous contours according to their relative orientation and position [17]. Because the contours extend the receptive field size of neurons in lower (occipital) visual processing regions, an integration across space, administered through parietal and frontal brain activity, is necessary for contour integration and detection [52]. The fact that partly different brain regions are involved into contour and non-contour processing makes the task suitable for a whole-brain classification analysis.

Previous neuroimaging results on contour integration suggest that both early retinotopic areas as well as higher visual brain sites contribute to contour processing. In a set of MRI adaptation studies Kourtzi and colleagues found that contours compared to

Table 3
Statistical measures evaluating classification results obtained with PCA and an RF classifier either without (exp. 1) or with (exp. 2) applying a linear Gaussian filter to the VIMFs.

RF						
	Experiment 1			Experiment 2		
	Acc ± std	Spec ± std	Sens ± std	Acc ± std	Spec ± std	Sens ± std
VIMF1	0.48 ± 0.02	0.47 ± 0.03	0.50 ± 0.03	0.53 ± 0.04	0.56 ± 0.04	0.51 ± 0.04
VIMF2	0.58 ± 0.02	0.63 ± 0.03	0.53 ± 0.03	0.51 ± 0.02	0.48 ± 0.03	0.53 ± 0.03
VIMF3	**0.75 ± 0.02**	**0.79 ± 0.04**	**0.71 ± 0.04**	**0.78 ± 0.02**	**0.81 ± 0.04**	**0.75 ± 0.04**
VIMF4	0.71 ± 0.02	0.71 ± 0.03	0.71 ± 0.03	0.73 ± 0.02	0.70 ± 0.03	0.77 ± 0.03
VIMF5	0.61 ± 0.02	0.57 ± 0.04	0.65 ± 0.04	0.47 ± 0.01	0.46 ± 0.02	0.48 ± 0.02
Res	0.65 ± 0.04	0.68 ± 0.05	0.61 ± 0.05	0.52 ± 0.03	0.57 ± 0.04	0.47 ± 0.04

Table 4
Statistical measures evaluating classification results obtained with ICA and an SVM classifier either without (exp. 1) or with (exp. 2) applying a linear Gaussian filter to the VIMFs.

SVM						
	Experiment 1			Experiment 2		
	Acc ± std	Spec ± std	Sens ± std	Acc ± std	Spec ± std	Sens ± std
VIMF1	0.67 ± 0.01	0.64 ± 0.03	0.70 ± 0.04	0.64 ± 0.03	0.65 ± 0.02	0.62 ± 0.05
VIMF2	0.69 ± 0.04	0.70 ± 0.07	0.68 ± 0.03	0.70 ± 0.03	0.70 ± 0.05	0.69 ± 0.04
VIMF3	**0.76 ± 0.03**	**0.78 ± 0.06**	**0.74 ± 0.03**	**0.73 ± 0.01**	**0.68 ± 0.00**	**0.77 ± 0.02**
VIMF4	0.70 ± 0.03	0.67 ± 0.04	0.73 ± 0.08	0.72 ± 0.04	0.68 ± 0.04	0.76 ± 0.04
VIMF5	0.70 ± 0.06	0.72 ± 0.06	0.68 ± 0.10	0.63 ± 0.02	0.63 ± 0.04	0.64 ± 0.04
Res	0.60 ± 0.02	0.66 ± 0.04	0.53 ± 0.02	0.62 ± 0.05	0.67 ± 0.03	0.56 ± 0.10

Table 5
Statistical measures evaluating classification results obtained with ICA and an RF classifier either without (exp. 1) or with (exp. 2) applying a linear Gaussian filter to the VIMFs.

RF						
	Experiment 1			Experiment 2		
	Acc ± std	Spec ± std	Sens ± std	Acc ± std	Spec ± std	Sens ± std
VIMF1	0.39 ± 0.01	0.41 ± 0.03	0.37 ± 0.02	0.44 ± 0.00	0.52 ± 0.00	0.36 ± 0.00
VIMF2	0.56 ± 0.02	0.59 ± 0.00	0.54 ± 0.05	0.42 ± 0.03	0.44 ± 0.02	0.50 ± 0.04
VIMF3	**0.70 ± 0.02**	**0.70 ± 0.03**	**0.66 ± 0.03**	**0.76 ± 0.03**	**0.77 ± 0.04**	**0.76 ± 0.03**
VIMF4	0.61 ± 0.02	0.52 ± 0.02	0.65 ± 0.02	0.74 ± 0.02	0.74 ± 0.04	0.74 ± 0.04
VIMF5	0.55 ± 0.04	0.56 ± 0.07	0.55 ± 0.03	0.40 ± 0.00	0.38 ± 0.00	0.42 ± 0.00
Res	0.66 ± 0.01	0.68 ± 0.00	0.65 ± 0.02	0.53 ± 0.00	0.47 ± 0.00	0.58 ± 0.00

non-contour patterns evoked increased BOLD responses all along earlier visual areas *V*1 to *V*4, as well as in lateral occipital and posterior fusiform areas within the inferior temporal lobe [28,2,3,27]. Other authors combined magneto- or electroencephalographic recordings (MEG/EEG) with source reconstruction methods to investigate the temporal dynamics and the neural sources of contour processing. They uniformly found that differences between contour and non-contour stimuli do not occur before 160 ms after stimulus onset, within the N1 to P2 time range of the event-related potentials or fields (ERP/ERF). The neural sources of the P1 / N1 differences were located within middle occipital [60,47] and occipito-temporal areas [57], as well as in primary visual cortex [47,57]. These results generally comply with the view that different visual areas contribute to contour perception. Additionally, due to the relatively late onset of ERP/ERF differences in primary visual areas, they suggest that the increased BOLD and ERP responses in early visual cortex during contour processing are mainly driven by feedback from higher visual sites.

Importantly, however, it is also true that neural responses to contour stimuli are highly variable across tasks. For example, the N1 ERP difference occurs later for misaligned compared to readily detectable contours [39], and differences between contour and non-contour stimuli can even be absent in untrained observers [32]. In order to explain the variability of brain responses, we need to consider that contours are no well-defined targets for detection.

Numerous instances of contours can occur during the experiment so that frequent updates of the target representation and the associated task are necessary for a successful contour detection. The updating and maintenance of task-related information, e.g. of task-related memories [55] or the task representation itself [58], are commonly considered frontal brain functions. In the present study we show for the first time that frontal brain activity alone, captured in VIMF2, performs reasonably as a classifier for contour and non-contour trials. The results thus underline the importance of frontal brain activity in contour integration and may mark a starting point for further investigations on that topic.

7. Conclusion

The investigation presented discusses the application of two-dimensional ensemble empirical mode decomposition (2DEEMD) to an fMRI study of a contour integration task. Because of the enormous computational load involved we currently only discussed data sets averaged over many trials and sessions. A systematic optimization of the parameters inherent to the method lead to a decomposition of whole brain scans into so-called volume modes, the equivalent of intrinsic mode functions in plain EMD, which exhibited characteristic textures on various spatial scales. Related activity distributions showed strong spatial localization and different modes exhibited activation in clearly separated areas of

the brain. Though in agreement with results of a canonical analysis with a GLM approach (using SPM 8), the 2DEEMD results show better localization, and activations appear more sparse and highly focused. Hence, the superior precision in spatial localization of activity blobs highlights the potential of 2DEEMD when analyzing functional imaging data sets. The evaluation of the classification performance based on *VIMFs*, most notably *VIMF*3 and *VIMF*4, also revealed a superior classification accuracy compared to "raw" data. Moreover, comparing two classifiers based on different principles, namely a RF and a SVM, the latter significantly outperforms a RF in terms of accuracy and ROC/AUC characteristics.

With respect to the perceptual task, there is a consensus that contour integration relies on distributed activity within higher as well as lower visual brain areas (e.g. [2,28]). However, a systematic investigation on whole-brain patterns of activity that might discriminate between contour and non-contour conditions has yet not been conducted. Our data show, for the first time, that distributed activity in bilateral inferior temporal (*VIMF*3) and superior occipital (*VIMF*4) lobe is maximally predictive for the stimulus condition. Moreover, we demonstrate that pre-frontal brain activity (*VIMF*2) discriminates between contour and non-contour patterns. The result adds up to those of previous fMRI studies [2,28]) and underlines the importance of higher brain areas for the perceptual integration of local stimulus details into a global form [27].

Generally, results clearly demonstrate the potential usefulness of a 2DEEMD analysis of functional imaging data [42]. A subsequent classification based on features generated from the intrinsic modes (*VIMFs*), extracted by 2DEEMD, relies on two feature characteristics: highly localized activity distributions in fMRI component images (*VIMFs*) compared to an GLM/SPM analysis, and a higher discriminating power compared to a classification of "raw" data sets.

Appendix A.

Both classifiers have been evaluated by repeating training and testing 10 times while employing a Leave-One-Out-Cross-Validation scheme and a random shuffling of the data sets presented to the classifiers. The number of features L in the SVM was varied while in the RF it was kept constant to $L = 38$.

References

[1] M.U. Altaf, T. Gautama, T. Tanaka, D.P. Mandic, Rotation invariant complex empirical mode decomposition, in: Proc. IEEE International Conference on Acoustics, Speech, Signal Processing, 2007.
[2] Ch.F. Altmann, H.H. Bülthoff, Z. Kourtzi, Perceptual organization of local elements into global shapes in the human visual cortex, Curr. Biol. 13 (4) (2003) 342–349.
[3] Ch.F. Altmann, A. Deubelius, Z. Kourtzi, Shape saliency modulates contextual processing in the human lateral occipital complex, J. Cogn. Neurosci. 16 (5) (2004) 794–804.
[4] N. Attoh-Okine, K. Barner, D. Bentil, R. Zhang, The empirical mode decomposition and the Hilbert–Huang transform, EURASIP J. Adv. Signal Process. (2008).
[5] S.M.A. Bhuiyan, R.R. Adhami, J.F. Khan, IEEE International Conference on Acoustics, Speech and Signal Processing ICASSP, 2009, pp. 1313–1316.
[6] S.M.A. Bhuiyan, J.F. Khan, N.O. Attoh-Okine, R.R. Adhami, Study of bidimensional empirical mode decomposition method for various radial basis function surface interpolators, in: In 2009 International Conference on Machine Learning and Applications, IEEE, 2009, pp. 18–24.
[7] Breiman Leo, Random forests, Mach. Learn. 45 (1) (2001) 5–32.
[8] V.D. Calhoun, T. Adali, L.K. Hansen, J. Larsen, J.J. Pekar, ICA of functional MRI data: an overview, in: Proceedings of the International Workshop on Independent Component Analysis and Blind Signal Separation, 2003, pp. 281–288.
[9] Ch.-Ch. Chang, Ch.-J. Lin, A Library for Support Vector Machines, 2001, available at http://www.csie.ntu.edu.tw/~cjlin/libsvm/.
[10] A. Cichocki, S. Amari, K. Siwek, T. Tanaka, Anh Huy Phan, et al., ICALAB Toolbox, 2007, available at http://www.bsp.brain.riken.jp/ICALAB/.
[11] A. Cichocki, R. Zdunek, A.H. Pham, S. Amari, Nonnegative Matrix and Tensor Factorizations Applications to Exploratory Multi-way Data Analysis and Blind Source Separation, Wiley and Sons, 2009.
[12] P. Common, Ch. Jutten, Handbook of Blind Source Separation: Independent Component Analysis and its Applications, Academic Press, 2010.
[13] Ch. Damerval, S. Meignen, V. Perrier, A fast algorithm for bidimensional EMD, IEEE Signal Process. Lett. 12 (10) (2005) 701–704.
[14] F. Deng, D. Zhu, L. Jinglei, L. Guo, T. Liu, FMRI signal analysis using empirical mean curve decomposition, IEEE TBME 60 (1) (2013) 42–54.
[15] A. Devor, E.M.C. Hillman, P. Tian, C. Waeber, I.C. Teng, L. Ruvinskaya, M.H. Shalinsky, H. Zhu, R.H. Haslinger, S.N. Narayanan, I. Ulbert, A.K. Dunn, E.H. Lo, B.R. Rosen, A.M. Dale, D. Kleinfeld, D.A. Boas, Stimulus-induced changes in blood flow and 2-deoxyglucose uptake dissociate in ipsilateral somatosensory cortex, J. Neurosci. 28 (2008) 14347–14357.
[16] Y. Fan, D. Shen, R.C. Gur, R.E. Gur, C. Davatzikos, COMPARE: classification of morphological patterns using adaptive regional elements, IEEE TMI 26 (1) (2007) 93–105.
[17] D.J. Field, A. Hayes, R.F. Hess, Contour integration by the human visual system: evidence for a local "association field", Vision Res. 33 (2) (1993) 173–193.
[18] P. Flandrin, G. Rilling, P. Goncalves, Empirical mode decomposition as a filter bank, IEEE Signal Process. Lett. 2 (2004) 112–114.
[19] J. Fleureau, A. Kachenoura, L. Albera, J.-C. Nunes, L. Senhadji, Multivariate empirical mode decomposition and application to multichannel filtering, Signal Process. 91 (12) (2011) 2783–2792.
[20] E. Haack, Magnetic Resonance Imaging, Physical Principles and Sequence Design, Wieley-Liss, 1999.
[21] S.J. Hanson, Y.O. Halchenko, Brain reading using full brain support vector machines for object recognition: there is no "face" identification area, Neural Comput. 20 (2008) 486–503.
[22] J.-D. Haynes, G. Rees, Decoding mental states from brain activity in humans, Nat. Rev. Neurosci. 7 (2006) 523–534.
[23] N.E. Huang, Z. Shen, S.R. Long, M.L. Wu, H.H. Shih, Q. Zheng, N.C. Yen, C.C. Tung, H.H. Liu, The empirical mode decomposition and Hilbert spectrum for nonlinear and nonstationary time series analysis, Proc. Roy. Soc. London A 454 (1998) 903–995.
[24] A. Jaiantilal, Classification and Regression by Randomforest-Matlab., 2009, available at https://code.google.com/p/randomforest-matlab/.
[25] A. Jaiantilal, http://code.google.com/p/randomforest-matlab/, 2010.
[26] S. Klöppel, C.M. Stonnington, C. Chu1, B. Draganski, R.I. Scahill, J.D. Rohrer, N.C. Fox, C.R. Jack, J. Ashburner, R.S.J. Frackowiak, Automatic classification of MR scans in Alzheimer's disease, Brain 131 (3) (2009) 681–689.
[27] Z. Kourtzi, E. Huberle, Spatiotemporal characteristics of form analysis in the human visual cortex revealed by rapid event-related fMRI adaptation, Neuroimage 28 (2) (2005) 440–452.
[28] Z. Kourtzi, A.S. Tolias, Ch.F. Altmann, M. Augath, N.K. Logothetis, Integration of local features into global shapes: monkey and human FMRI studies, Neuron 37 (2) (2003) 333–346.
[29] N. Kriegeskorte, R. Goebel, P. Bandettini, Information-based functional brain mapping, Proc. Natl. Acad. Sci. 103 (2006) 3863–3868.
[30] E.W. Lang, R. Schachtner, D. Lutter, D. Herold, A. Kodewitz, F. Blöchl, F.J. Theis, I.R. Keck, J.M. Górriz Sáez, P. Gómez Vilda, A.M. Tomé, Exploratory Matrix Factorization Techniques for Large Scale Biomedical Data Sets, Bentham Science Publishers, 2010.
[31] Z. Lao, Morphological classification of brains via high-dimensional shape transformations and machine learning methods, NeuroImage 21 (2004) 46–57.
[32] Wu Li, Valentin Piëch, Charles D. Gilbert, Learning to link visual contours, Neuron 57 (3) (2008) 442–451.
[33] A. Linderhed, 2-D empirical mode decompositions in the spirit of image compression, in: Wavelet and Independent Component Analysis Applications IX, Proceedings of SPIE, vol. 4738, 2002, pp. 1–8.
[34] Z. Liu, S. Peng, Boundary processing of bidimensional EMD using texture synthesis, IEEE Signal Process. Lett. 12 (2005) 33–36.
[35] Z. Liu, H. Wang, S. Peng, Texture classification through directional empirical mode decomposition, in: Proc. 17th IEEE International Conference on Pattern Recognition (ICPR'04), 2004, pp. 803–806.
[36] Z. Liu, H. Wang, S. Peng, Texture segmentation using directional empirical mode decomposition, in: Proceedings of IEEE International Conference on Image Processing (ICIP'04), 2004, pp. 279–282.
[37] S.R. Long, Applications of HHT in Image Analysis, World Scientific, River Edge, NJ, USA, 2005, pp. 289–305.
[38] D. Looney, D.P. Mandic, Multi-scale image fusion using complex extensions of EM, IEEE Trans. Signal Process. 57 (4) (2009) 1626–1630.
[39] Birgit Mathes, Dennis Trenner, Fahle Manfred, The electrophysiological correlate of contour integration is modulated by task demands, Brain Res. 1114 (1) (2006) 98–112.
[40] MATLAB and Statistics Toolbox. Release 2013, 2013.
[41] J. Mourao-Miranda, A.L.W. Bokde, C. Born, H. Hampel, M. Stetter, Classifying brain states and determining the discriminating activation patterns: support vector machine on functional MRI data, NeuroImage 28 (2005) 980–995.
[42] A. Neubauer, A. Tomé, A. Kodewitz, J. Górriz, G. Puntonet, E. Lang, Bidimensional ensemble empirical mode decomposition of functional biomedical images, Adv. Adaptive Data Anal. 06 (2014) 1450004, 36 pages.
[43] K.A. Norman, S.M. Polyn, G.J. Detre, J.V. Haxby, Beyond mind-reading: multivoxel pattern analysis of fMRI data, Trends Cogn. Sci. 10 (2006) 424–430.
[44] J.C. Nunes, Y. Bouaoune, E. Delechelle, O. Niang, Ph Bunel, Image analysis by bidimensional empirical mode decomposition, Image Vis. Comput. 21 (12) (2003) 1019–1026.
[45] J.C. Nunes, E. Deléchelle, Empirical mode decomposition: applications on signal and image processing, Adv. Adaptive Data Anal. 1 (2009) 125–175.

[46] J.C. Nunes, S. Guyot, E. Deléchelle, Texture analysis based on local analysis of the bidimensional empirical mode decomposition, Mach. Vision Appl. 16 (2005) 177–188.

[47] M.A. Pitts, A. Martínez, S.A. Hillyard, Visual processing of contour patterns under conditions of inattentional blindness, J. Cogn. Neurosci. 24 (2) (2012) 287–303.

[48] N. Rehman, D.P. Mandic, Empirical mode decomposition for trivariate signals, IEEE Trans. Signal Process. 58 (3) (2010) 1059–1068.

[49] N. Rehman, D.P. Mandic, Multivariate empirical mode decomposition, Proc. Roy. Soc. A 466 (2010) 1291–1302.

[50] N. Rehman, D.P. Mandic, Quadrivariate empirical mode decomposition, in: International Joint Conference on Neural Networks (IJCNN 2010), 2010, pp. 1–7.

[51] G. Rilling, P. F1andrin, P. Goncalves, J.M. Lilly, Bivariate empirical mode decomposition, IEEE Signal Process. Lett. 14 (2007) 936–939.

[52] P.R. Roelfsema, Cortical algorithms for perceptual grouping, Ann. Rev. Neurosci. 29 (2006) 203–227.

[53] A. Rojas, J.M. Górriz, J. Ramírez, I.A. Ill'an, F.J. Martínez Murcia anmd, A. Ortiz, M. Gómez Río, M. Moreno, Caballero, Application of empirical mode decomposition (EMD) on DaTSCAN SPECXT images to explore Parkinson disease, Expert Syst. Appl. 40 (2013) 2756–2766.

[54] Ch. Rorden, Mricro, 2012, available at http://www.nitrc.org/projects/mricron.

[55] Armin Schnider, Valerie Treyer, Alfred Buck, Selection of currently relevant memories by the human posterior medial orbitofrontal cortex, J. Neurosci. 20 (15) (2000) 5880–5884.

[56] Bernhard Schölkopf, Alexander J. Smola, Learning with Kernels, The MIT Press, 2002.

[57] M. Shpaner, S. Molholm, E. Forde, J.J. Foxe, Disambiguating the roles of area V1 and the lateral occipital complex (LOC) in contour integration, NeuroImage 69 (2013) 146–156.

[58] Stoet Gijsbert, Lawrence H. Snyder, Neural correlates of executive control functions in the monkey, Trends Cogn. Sci. 13 (5) (2009) 228–234.

[59] T. Tanaka, D.P. Mandic, Complex empirical mode decomposition, IEEE Signal Process. Lett. 14 (2) (2006) 101–104.

[60] T. Tanskanen, J. Saarinen, L. Parkkonen, R. Hari, From local to global: cortical dynamics of contour integration, J Vis. 8 (7) (2008), 15. 1-1512.

[61] P. Vemuri, J.L. Gunter, M.L. Senjem, J.L. Whitwell, K. Kantarci, D.S. Knopman, B.F. Boeve, R.C. Petersen Jr., C.R. Jack, Alzheimer's disease diagnosis in individual subjects using structural MR images: validation studies, NeuroImage 39 (3) (2008) 1186–1197.

[62] E. Webster, Medical Instrumentation: Application and Design, John Wiley & Sons, Inc., 1998.

[63] Zh. Wu, N.E. Huang, Ensemble empirical mode decomposition: a noise-assisted data analysis method, Adv. Adaptive Data Anal. 1 (1) (2009) 1–41.

[64] Zh. Wu, N.E. Huang, X. Chen, The multidimensional ensemble empirical mode decomposition method, Adv. Adaptive Data Anal. 1 (2009) 339–372.

[65] Ch.-Zh. Xiong, J.y. Xu, J.-Ch. Zou, D.-X. Qi, Texture classification based on EMD and FFT, J. Zhejiang Univ. – Sci. A 7 (2006) 1516–1521, 10.1631/jzus.2006.A1516.

[66] Y. Xu, B. Liu, J. Liu, S. Riemenschneider, Two-dimensional empirical mode decomposition by finite elements, Proc. Roy. Soc. A 462 (2006) 3081–3096.

[67] Omar Ait Zemzami, Hamid Akasse, Mohammed Ouanan, Brahim Akasse, Benkider Aziza, Decomposition of 3D medical image based on fast and adaptive bidimenisional empirical mode decomposition, Int. J. Comput. Networks Commun. Sec. 7 (2013) 299–309.

[68] J.Z. Zhang, Z. Qin, Edge detection using fast Bidimensional Empirical Mode Decomposition and mathematical morphology, in: Proceedings of the IEEE SoutheastCon (SoutheastCon), 2010, pp. 139–142.

[69] T. Zheng, M. Cai, T. Jiang, A novel approach to activation detection in fMRI based on empirical mode decomposition, J. Integrative Neurosci. 9 (4) (2010) 407–427.